

Successive magnetic transitions and spin structure in the two-leg ladder compound CsFe_2Se_3 observed by ^{133}Cs and ^{77}Se NMR

Mina Murase,¹ Kaoru Okada,¹ Yoshiaki Kobayashi,¹ Yasuyuki Hirata,² Kazuki Hashizume,³ Takuya Aoyama,³ Kenya Ohgushi,³ and Masayuki Itoh¹

¹*Department of Physics, Graduate School of Science, Nagoya University, Furo-cho, Chikusa-ku, Nagoya 464-8602, Japan*

²*Institute for Solid State Physics, University of Tokyo, 5-1-5 Kashiwanoha, Kashiwa 277-8581, Japan*

³*Department of Physics, Graduate School of Science, Tohoku University, 6-3 Aramaki Aza-Aoba, Aoba-ku, Sendai 980-8578, Japan*

 (Received 24 April 2020; revised 26 June 2020; accepted 30 June 2020; published 20 July 2020)

^{133}Cs and ^{77}Se NMR measurements were conducted on a single crystal to study the local magnetic and electronic properties of the Fe-based compound CsFe_2Se_3 with a two-leg ladder structure. From the experimental results of the ^{133}Cs and ^{77}Se NMR spectra and the ^{133}Cs nuclear spin-lattice relaxation rate, we found successive magnetic transitions from a paramagnetic phase to an incommensurate-like antiferromagnetic (AFM1) phase with a distributed internal field at $T_{N1} = 176.5$ K and then from the AFM1 phase to another commensurate antiferromagnetic (AFM2) phase at $T_{N2} = 148.5\text{--}152.0$ K. Internal fields of the Cs and Se sites obtained from the angular dependence of the NMR spectra are discussed in terms of the transferred hyperfine tensors governed by site symmetry. For the AFM2 phase, we show that the stripe-type spin structure occurs in two domains, which have magnetic wave vectors of $\mathbf{Q} = (1/2, 1/2, 0)$ and $(1/2, -1/2, 0)$. On the contrary, we observed a characteristic modulation of the internal field with magnetic fluctuation between the ladders in the AFM1 phase. To clarify why CsFe_2Se_3 has a large charge gap although it is a $\text{Fe}^{2.5+}$ mixed valent compound, we investigated the hyperfine coupling constants and found that a hole is doped into the Fe site instead of the Se site. Based on this fact, molecular orbital and double exchange models are proposed for the electronic state.

DOI: [10.1103/PhysRevB.102.014433](https://doi.org/10.1103/PhysRevB.102.014433)

I. INTRODUCTION

Since the discovery of the Fe-based superconductor $\text{LaFeAsO}_{1-x}\text{F}_x$ [1], a number of Fe-based compounds have been considered for the development of new superconductors and related compounds. One compound is the Fe-based ladder insulating system AFe_2X_3 ($A = \text{Ba, K, Rb, Cs}$; $X = \text{S, Se, Te}$) [2–6]. The superconducting (SC) transitions recently discovered at high pressures in BaFe_2S_3 [7,8] and BaFe_2Se_3 [9] have attracted significant attention in terms of the SC mechanism. These compounds have unique spin structures related to those in parent compounds of Fe-based superconductors, which typically show a stripe-type antiferromagnetic (AFM) order. The stripe-type AFM order has been discussed from an itinerant viewpoint where the nesting plays a key role on the Fermi surface with electron and hole pockets [10–12]. The other viewpoint is a localized one, where the nearest-neighbor (nn) and next-nearest-neighbor (nnn) AFM interactions compete with each other [13–18]. Among the AFe_2X_3 variants, BaFe_2Se_3 has a block-type structure, where four neighboring Fe spins in the two-leg ladder form a ferromagnetic (FM) quadratic block and the neighboring FM blocks are antiferromagnetically coupled [5,19–22]. However, BaFe_2S_3 and CsFe_2Se_3 show stripe-type structures, where the magnetic moments couple ferromagnetically along the rung direction and antiferromagnetically along the leg direction [6,22,23]. The characteristic spin structures appear in the parent compounds of Fe-based superconductors. Based on five- and two-orbital models for the two-leg ladder compounds,

the phase diagram was studied using several many-body techniques, and several spin structures were found to appear dependently on the electron number [24–26]. A temperature T and composition phase diagram was also investigated for $\text{Ba}_{1-x}\text{Cs}_x\text{Fe}_2\text{Se}_3$ [27]. Thus, the magnetic properties of AFe_2X_3 are expected to provide valuable information on such Fe-based superconductors.

CsFe_2Se_3 crystallizes in the orthorhombic structure (space group $Cmcm$), as shown in Fig. 1 [3,6]. As can be seen, the edge-shared FeSe_4 tetrahedra form two-leg ladders along the c axis. Furthermore, there are one Fe, one Cs, and two Se (Se1 and Se2) sites. In BaFe_2Se_3 with Fe^{2+} , the coexistence of itinerant and localized Fe electrons was proposed based on photoemission and resonant inelastic x-ray scattering studies [28,29]. Although CsFe_2Se_3 has a formal Fe valence of $+2.5$, it has the largest charge gap among these systems. In a photoemission spectroscopic study, the insulating state of CsFe_2Se_3 was explained by the localization of a hole at the Se site [6,28]. From x-ray absorption and inelastic resonant scattering spectroscopy, the FM molecular orbital with a doped hole was inferred to be realized along the rungs [22], thereby conflicting with the model of a doped hole in the Se site. Thus, the hole location remains controversial. In CsFe_2Se_3 , the coexistence of paramagnetic (PM) and AFM phases was observed in a Mössbauer experiment when the value of T_N was below 175 K [6]. Stripe-type spin structure with the magnetic wave vector $\mathbf{Q} = (1/2, 1/2, 0)$ below T_N was also proposed based on a neutron scattering measurement [6]. However, the anomalous behavior, such as the coexistence of the PM and

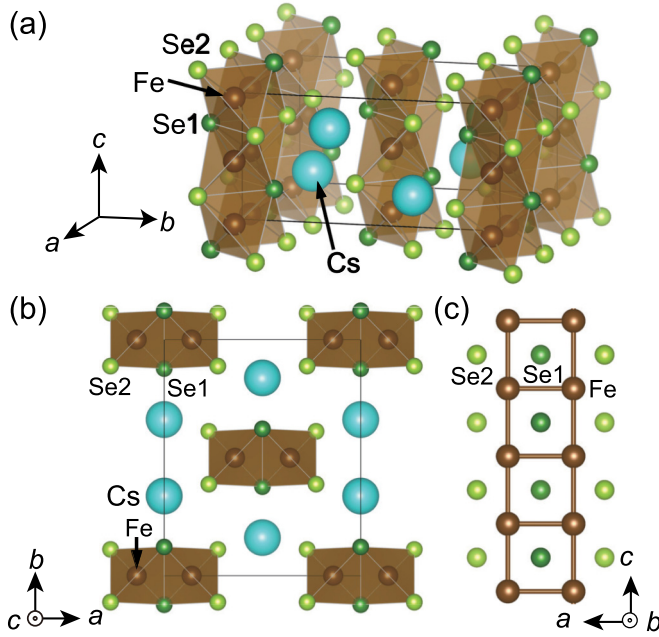


FIG. 1. (a) Crystal structure of CsFe_2Se_3 . (b) Crystal structure projected on the ab plane. (c) Ladder structure composed of edge-shared FeSe_4 tetrahedra projected on the ca plane. The rectangular parallelepiped and rectangle each represent a unit cell.

AFM phases, has not yet been investigated from a microscopic viewpoint.

Nuclear magnetic resonance (NMR) is a useful tool for studying the local magnetic properties of materials. In this study we conducted ^{133}Cs and ^{77}Se NMR measurements on a single crystal to investigate the magnetic and electronic properties of the Fe-based compound CsFe_2Se_3 with having a ladder structure. Successive changes in the ^{133}Cs and ^{77}Se NMR spectra and the ^{133}Cs nuclear-spin lattice relaxation rate $1/T_1$ were observed to appear owing to the magnetic transitions from the PM phase to an AFM phase at $T_{N1} = 176.5$ K (AFM1) and from the AFM1 phase to another AFM phase at $T_{N2} = 148.5\text{--}152.0$ K (AFM2). In particular, the present NMR study is the first to observe the transition at T_{N2} . Even in the newly found AFM1 phase, no observation of the NMR spectrum from the PM region excludes the model of the coexistence of the PM and AFM phases. The detailed analysis of the NMR spectra based on transferred hyperfine (TH) interaction and site symmetry enables us to obtain the internal fields at the Cs and Se sites of the AFM1 and AFM2 phases. Based on them, we find an incommensurate structure in the AFM1 phase and a commensurate spin structure with two stripe-type domains in the AFM2 phase. The successive magnetic transitions are thought to be attributable to the magnetic frustration effect, which may lead to the presence of two-type domains in the AFM2 phase and the remaining magnetic fluctuation in the AFM1 phase. Based on the analysis of the TH coupling constants, we conclude that there is no doping of a hole into the Se site, which is clearly inconsistent with the model of a hole in the Se site. Based on this fact, molecular orbital and double exchange models are proposed for the electronic state.

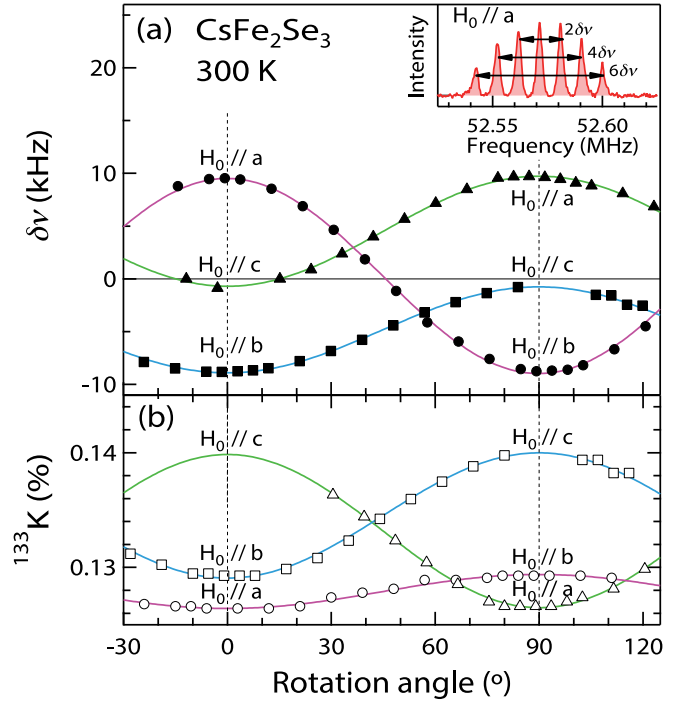


FIG. 2. Angular dependence of (a) ^{133}Cs nuclear quadrupole splitting $\delta\nu$ and (b) ^{133}Cs Knight shift ^{133}K at 300 K with $H_0 = 9.4031$ T rotated within the ab , bc , and ca planes in the CsFe_2Se_3 single crystal. The inset shows the ^{133}Cs NMR spectrum with H_0 parallel to the a axis. The curves are the results of the experimental data fitted to Eqs. (1) and (2) with the parameter values in the text and Table I, respectively.

II. EXPERIMENTAL PROCEDURE

A CsFe_2Se_3 single crystal was grown by the melt-growth method [6,30,31]. NMR measurements were conducted using a conventional pulsed spectrometer. A single crystal of CsFe_2Se_3 with a size of $2 \times 2 \times 0.1$ mm³ was utilized for the experiment. Fourier-transformed spectra were obtained for spin-echo signals in magnetic fields of $H_0 = 5.8705$, 8.8012, 9.4031, and 11.4995 T. A ^{133}Cs nucleus has a nuclear spin of $^{133}I = 7/2$ and nuclear gyromagnetic ratio of $^{133}\gamma_n = 2\pi \times 5.5844$ MHz/T, whereas those of an ^{77}Se nucleus are $^{77}I = 1/2$ and $^{77}\gamma_n = 2\pi \times 8.119$ MHz/T, respectively. A two-axis goniometer was utilized to precisely rotate the single crystal in the magnetic field. The ^{133}Cs nuclear spin-lattice relaxation rate $1/T_1$ was measured using the inversion-recovery method.

III. EXPERIMENTAL RESULTS

A. ^{133}Cs NMR

We observed the ^{133}Cs NMR spectrum at 300 K with $H_0 = 9.4031$ T parallel to the a axis in the CsFe_2Se_3 single crystal, as presented in the inset of Fig. 2(a). The spectrum was composed of seven lines split by the electric quadrupole interaction for $I = 7/2$. Figure 2(a) shows the angular dependence of the electric quadrupole splitting, $\delta\nu = (\nu_{m \leftrightarrow m-1} - \nu_{-m+1 \leftrightarrow -m}) / (2m - 1)$, ($m = I, I - 1, \dots, 3/2$), where $\nu_{m \leftrightarrow m-1}$ is the resonance frequency of the $m \leftrightarrow m - 1$ satellite line, with H_0 rotated in the

TABLE I. ^{133}Cs Knight shifts $^{133}K_{xx}$, $^{133}K_{yy}$, and $^{133}K_{zz}$ and the isotropic one $^{133}K_{\text{iso}}$, axially anisotropic one $^{133}K_{\text{ax}}$, and in-plane anisotropic one $^{133}K_{\text{aniso}}$ at 300 K in CsFe_2Se_3 . All the Knight shifts are given as percentages.

$^{133}K_{xx}$	$^{133}K_{yy}$	$^{133}K_{zz}$	$^{133}K_{\text{iso}}$	$^{133}K_{\text{ax}}$	$^{133}K_{\text{aniso}}$
0.127	0.129	0.140	0.132	0.004	0.001

ab , bc , and ca planes. The averaged $\delta\nu$ data for $m = 7/2$, $5/2$, and $3/2$ are presented in Fig. 2(a). In the first-order perturbation of the electric quadrupole interaction, $\delta\nu$ is expressed as [32]

$$\delta\nu = \frac{1}{2}\nu_Q(3\cos^2\theta - 1 + \eta\sin^2\theta\cos 2\phi), \quad (1)$$

where θ is the polar angle from the principal z axis, and ϕ is the azimuth angle from the principal x axis in the xyz principal coordinate system of the electric field gradient (EFG) tensor. The nuclear electric quadrupole frequency ν_Q is defined as $\nu_Q = 3eQV_{zz}/[2I(2I - 1)\hbar]$ with elementary charge e , nuclear quadrupole moment Q , Plank's constant \hbar , and a component of the EFG tensor $V_{\alpha\beta}$ ($\alpha, \beta = x, y, z$). The asymmetry parameter of EFG, η , is defined as $\eta = |V_{xx} - V_{yy}|/|V_{zz}|$ ($|V_{xx}| \leq |V_{yy}| \leq |V_{zz}|$). The experimental data of $\delta\nu$ in Fig. 2(a) are well reproduced by Eq. (1) with $\nu_Q = 9.6$ kHz and $\eta = 0.85$. The principal x , y , and z axes are the c , b , and a axes, respectively. This result is consistent with the local symmetry at the Cs site on the mirror ab and bc planes.

Figure 2(b) shows the angular dependence of the ^{133}Cs Knight shift ^{133}K determined by the center line at 300 K. Here, a slight correction owing to a demagnetization field is performed. In general, the Knight shift K is expressed in the xyz principal coordinate system as [32]

$$K = K_{xx}\sin^2\theta\cos^2\phi + K_{yy}\sin^2\theta\sin^2\phi + K_{zz}\cos^2\theta, \quad (2)$$

where K_{xx} , K_{yy} , and K_{zz} are the principal values of the Knight shift tensor. From fitting the experimental data to Eq. (2), we obtained the principal values $^{133}K_{xx}$, $^{133}K_{yy}$, and $^{133}K_{zz}$, which are listed with the isotropic component $^{133}K_{\text{iso}} = (^{133}K_{xx} + ^{133}K_{yy} + ^{133}K_{zz})/3$, axially anisotropic one $^{133}K_{\text{ax}} = (2^{133}K_{zz} - ^{133}K_{xx} - ^{133}K_{yy})/6$, and in-plane anisotropic one $^{133}K_{\text{aniso}} = (^{133}K_{yy} - ^{133}K_{xx})/2$ in Table I. The principal x , y , and z axes are the a , b , and c axes, respectively. Thus, ^{133}K primarily has the $^{133}K_{\text{iso}}$ component, which may originate from the TH interaction between the ^{133}Cs nucleus and its neighboring Fe ions via the mixing of the Fe $3d$ and Cs s orbitals and/or polarization of inner core s electrons via the Se $4p$ orbitals.

In Fig. 3(a) the T dependence of the ^{133}Cs NMR spectrum with $H_0 = 5.8705$ T parallel to the a axis in the T range of 100–180 K is examined. The spectrum drastically changes at $T_{N1} = 176.5$ K, below which a double horn structure appears. It can be observed that the electric quadrupole splitting is masked behind the spectrum width below T_{N1} . The splitting between the horns increases with decreasing T . Furthermore, at $T_{N2} \sim 149$ K, the spectrum again changes from horn shaped to peak shaped, as shown in Fig. 3(a). To more clearly observe the change in the spectral shape around T_{N2} , we measured the ^{133}Cs NMR spectrum for $H_0 = 8.8012$ T parallel to the

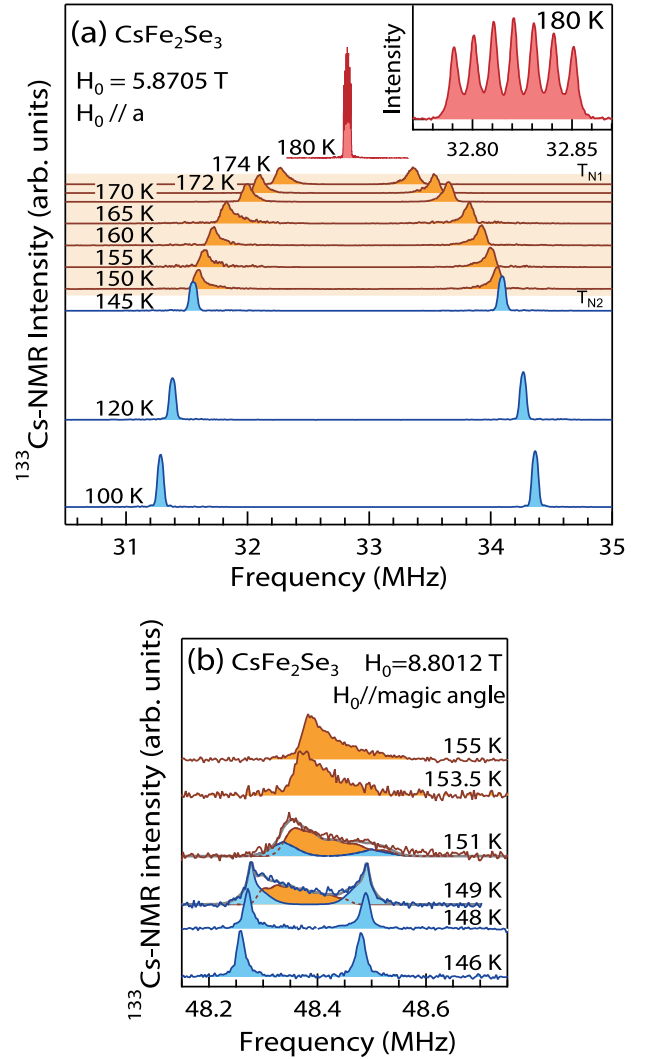


FIG. 3. Temperature dependence of the ^{133}Cs NMR spectrum with (a) $H_0 = 5.8705$ T parallel to the a axis and (b) $H_0 = 8.8012$ T parallel to the direction 45° from the a axis, corresponding to a magic angle in the CsFe_2Se_3 single crystal. The inset in (a) shows the expanded NMR spectrum at 180 K. Only spectra located at lower frequencies are presented around T_{N2} in (b). Each of the spectra at 149 and 151 K can be divided into two spectra originating from the AFM1 and AFM2 regions by simulation, as presented by the ocher and light blue spectra, respectively.

direction of 45° from the a axis in the ab plane, corresponding to a magic angle where the electric quadrupole splitting vanishes. Here the higher field was utilized to obtain a good signal/noise ratio for the spectrum. The measured spectrum is presented in Fig. 3(b), the spectrum is only shown at lower frequencies. Across T_{N2} , the horn changes to two peaks, and T ranges from 148.5 to 152.0 K, where the spectra above and below T_{N2} coexist as the simulated ocher and light blue spectra, respectively, as shown in Fig. 3(b). These changes in the spectra imply that the successive magnetic transitions take place from the PM phase to the AFM1 phase at T_{N1} and from the AFM1 phase to the AFM2 phase at T_{N2} . The fact that the ^{133}Cs NMR spectrum from the PM region is not observed below T_{N1} indicates that there is no coexistence of the PM and

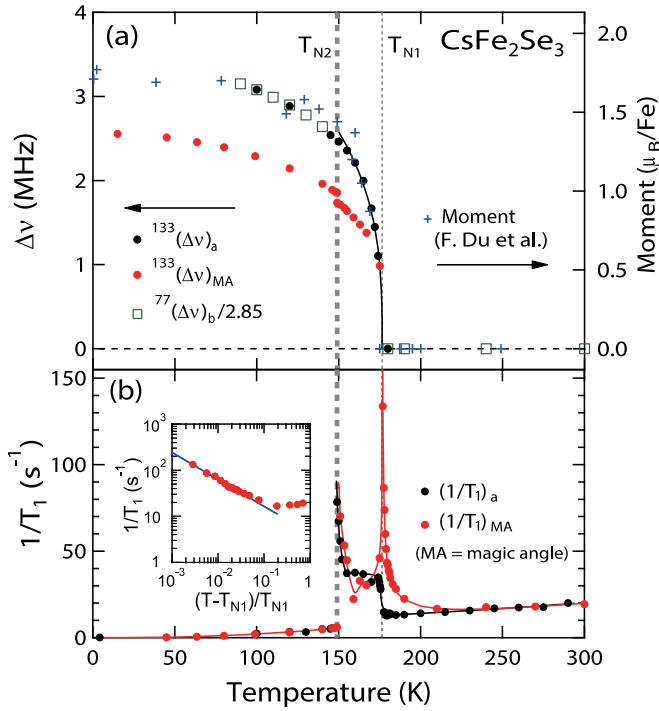


FIG. 4. (a) Temperature dependence of the frequency difference between the horns in the T range of $T_{N2} < T < T_{N1}$ and the peaks below T_{N2} in the ^{133}Cs NMR spectrum for $H_0 = 5.8705$ T parallel to the a axis $^{133}(\Delta\nu)_a$ and $H_0 = 8.8012$ T parallel to the magic angle $^{133}(\Delta\nu)_{MA}$ and between the peaks below T_{N2} in the ^{77}Se NMR spectrum from the Se2 site for $H_0 = 5.8705$ T parallel to the b axis $^{77}(\Delta\nu)_b$ in the CsFe_2Se_3 single crystal. The $\Delta\nu = 0$ data above T_{N1} are also plotted. (b) Temperature dependence of the ^{133}Cs nuclear spin-lattice relaxation rate $1/T_1$ with H_0 parallel to the a axis $(1/T_1)_a$ and the magic angle $(1/T_1)_{MA}$. The blue pluses in (a) are the experimental data of the sublattice magnetization measured by neutron scattering [6]. The curve in (a) shows the relation $^{133}(\Delta\nu)_a \propto [(T_{N1} - T)/T_{N1}]^\beta$ with $T_{N1} = 176.5$ K and $\beta = 0.33$. The inset plots $1/T_1$ versus $(T - T_{N1})/T_{N1}$, where the solid line represents the fitted result of the $(1/T_1)_{MA}$ data to the relation $(1/T_1)_{MA} \propto [(T - T_{N1})/T_{N1}]^{-\gamma}$ with $T_{N1} = 176.5$ K and $\gamma = 0.59$. The solid curves in (b) are for ease of visualization.

AFM regions. Thus, this excludes the model of the coexistence based on the Mössbauer experiment [6]. Furthermore, the transition at T_{N2} using the neutron scattering measurement was also not observed [24], and this is considered to have originated from its resolution limit, as there is a slight variation in the magnetization at T_{N2} . Figure 4(a) shows the T dependence of the frequency difference between the horns in the range $T_{N2} < T < T_{N1}$ and the peaks below T_{N2} , $\Delta\nu$. $\Delta\nu$ in the ^{133}Cs spectrum of $H_0 \parallel a$, $^{133}(\Delta\nu)_a$, rapidly increases owing to the AFM order with T decreasing below $T_{N1} = 176.5$ K, which is determined by $1/T_1$, as mentioned below, and can be fitted to the relation $^{133}(\Delta\nu)_a \propto [(T_{N1} - T)/T_{N1}]^\beta$ with the critical exponent $\beta = 0.33 \pm 0.02$, as shown in Fig. 4(a). Additionally, $\Delta\nu$ exhibits a T dependence that follows the order parameter of the sublattice magnetization observed by neutron scattering [6]. While $^{133}(\Delta\nu)_a$ shows no drastic change at T_{N2} , the ^{133}Cs NMR spectra from the AFM1 and AFM2 regions (simulated

other and light blue spectra, respectively), for H_0 parallel to the magic angle coexist in the T range of 148.5–152.0 K, as shown in Fig. 3(b). Additionally, $\Delta\nu$ between the outer peaks for H_0 parallel to the magic angle, $^{133}(\Delta\nu)_{MA}$, clearly shows a slight jump at T_{N2} , as shown in Fig. 4(a). These observations show that the first-order transition takes place from the AFM1 phase to AFM2 phase.

These successive transitions are also clearly observed by the ^{133}Cs nuclear spin-lattice relaxation rate $1/T_1$. We measured $1/T_1$ for H_0 parallel to the a axis, $(1/T_1)_a$, and the magic angle where the electric quadrupole splitting effect vanishes, $(1/T_1)_{MA}$, near the [110] direction, where the single exponential decay of the ^{133}Cs nuclear magnetization was observed. The small quadrupole splitting did not prevent the successful observation of the single exponential decay even for $H_0 \parallel a$ in the PM and AFM2 phases, whereas it was observed to follow the summation of two exponential functions with short and long T_1 values due to a distribution of the internal field in the AFM1 phase even for H_0 parallel to the magic angle. Figure 4(b) shows the T dependencies of $(1/T_1)_a$ and $(1/T_1)_{MA}$. Here the long T_1 data are presented in the AFM1 phase. At T_{N1} , $(1/T_1)_{MA}$ shows a divergent behavior due to critical slowing down. In the critical region, the experimental data of $(1/T_1)_{MA}$ above T_{N1} can be fitted to the relation $(1/T_1)_{MA} \propto [(T - T_{N1})/T_{N1}]^{-\gamma}$, as presented in the inset of Fig. 4(b). We obtained the critical exponent $\gamma = 0.59 \pm 0.12$ and $T_{N1} = 176.5 \pm 0.1$ K. In the AFM1 phase, $(1/T_1)_{MA}$ remains finite and increases towards T_{N2} with decreasing T , whereas it rapidly reduces below T_{N2} . However, $(1/T_1)_a$ shows no critical behavior slightly above T_{N1} , a step below T_{N1} , and an increase near T_{N2} ; it rapidly drops below T_{N2} .

In a magnetically ordered phase, the internal field H_{in} leads to the angular dependence of the NMR spectrum that is dependent on the spin structure. Figures 5(a)–5(c) show the angular dependencies of the ^{133}Cs NMR spectrum for $H_0 = 5.8705$ T parallel to the bc , ca , and ab planes, respectively, at 170 K in the AFM1 phase. The double horn structure has a characteristic broadening that is dependent on the direction of the magnetic field. On the contrary, Figs. 5(d)–5(f) show angular dependencies of the ^{133}Cs NMR spectrum for $H_0 \parallel bc$, ca , and ab , respectively, at 120 K in the AFM2 phase. The double horn structure changes to a peak structure below T_{N2} . Two peaks appear for $H_0 \parallel bc$ and ca , whereas there are four peaks for $H_0 \parallel ab$. In general, the NMR frequency in a magnetically ordered phase ν_{res} is expressed as

$$\nu_{\text{res}} = \frac{\gamma_n}{2\pi} \sqrt{H_0^2 + H_{in}^2 - 2H_0H_{in}\cos\psi}, \quad (3)$$

where ψ is the angle between H_0 and H_{in} . In the AFM2 phase of CsFe_2Se_3 , the experimental data for $H_0 \parallel ab$ are well fitted to Eq. (3) with $\psi = \theta_c - \theta_{c,0}$ where θ_c ($\theta_{c,0}$) is the angle of H_0 (H_{in}) from the a axis in the ab plane, as presented in Fig. 5(c). From the experimental data fitted to Eq. (3), we can obtain the internal fields of the Cs site listed in Table II. Note that all choices of sign are independent, giving four vectors for the Cs site. Thus, the Cs site has four H_{in} vectors, as shown by the black arrows in the inset of Fig. 5(d). The internal fields at 120 K have an absolute value of 2.54 kOe and are parallel to the directions of $\theta_{c,0} = \pm 7^\circ$ and $\pm 173^\circ$ in the ab plane.

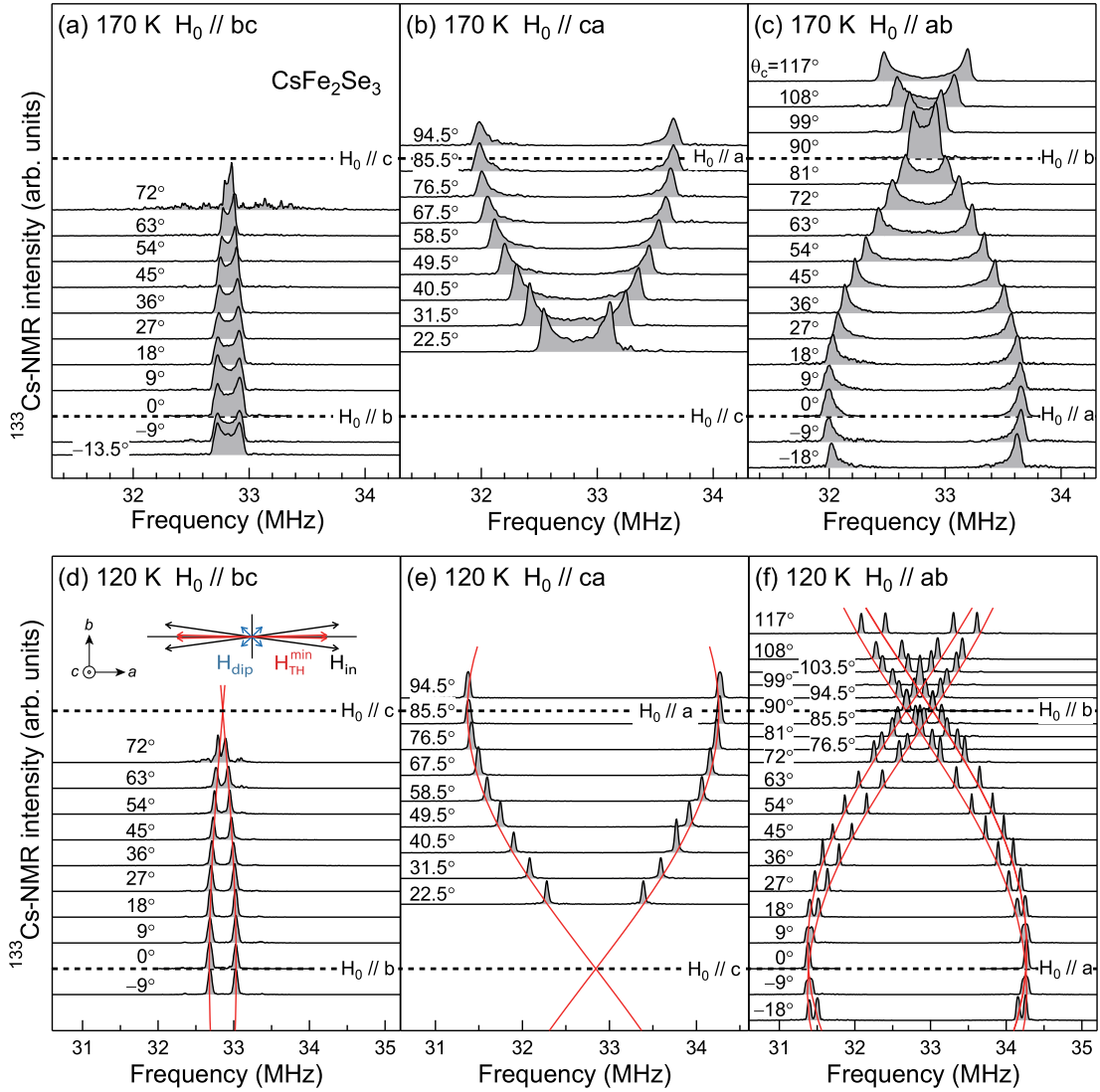


FIG. 5. Angular dependence of the ^{133}Cs NMR spectrum with $H_0 = 5.8705$ T rotated in the (a) bc , (b) ca , and (c) ab planes at 170 K, and in the (d) bc , (e) ca , and (f) ab planes at 120 K in the CsFe_2Se_3 single crystal. The solid red curves are the results of fitting the data to Eq. (3) with the internal fields listed in Table II. The inset of (d) shows the internal field H_{in} (black arrow), dipole field H_{dip} (blue arrow) calculated for the spin structure in Fig. 13(a), and transferred hyperfine field $H_{\text{TH}}^{\text{min}}$ (red arrow) of the Cs positions at 120 K.

B. ^{77}Se NMR

^{77}Se NMR is advantageous in the investigation of the valence state at the Se sites in CsFe_2Se_3 . The inset of Fig. 6(a)

shows the ^{77}Se NMR spectrum at 300 K with $H_0 = 5.8705$ T parallel to the b axis. We obtained the angular dependencies of the ^{77}Se Knight shift ^{77}K at 300 K with $H_0 = 5.8705$ T

TABLE II. The internal field H_{in} observed in the present NMR measurement, the dipole field H_{dip} calculated with the Fe magnetic moment of $1.5 \mu_{\text{B}}$ for the spin structure presented in Figs. 13(a) and 13(b), and calculated transferred hyperfine fields with minimum absolute value ($H_{\text{TH}}^{\text{min}}$) and maximum absolute value ($H_{\text{TH}}^{\text{max}}$) for the Cs, Se1, and Se2 sites at 120 K in the AFM2 phase of CsFe_2Se_3 . All choices of sign are independent, giving four vectors for the Cs and Se1 sites and eight vectors for the Se2 site. The vector components are expressed in the abc coordinate system.

Site	H_{in} (kOe) (Expt.)	H_{dip} (kOe) (Calc.)	$H_{\text{TH}}^{\text{min}}$ (kOe) (Calc.)	$H_{\text{TH}}^{\text{max}}$ (kOe) (Calc.)
Cs	$\pm(2.52, \pm 0.31, 0)$	$\pm(0.33, \pm 0.27, 0)$	$\pm(2.19, \pm 0.04, 0)$	$\pm(2.85, \pm 0.58, 0)$
Se1	$\pm(\pm 0.24, 5.15, 0)$	$\pm(\pm 0.03, 3.49, 0)$	$\pm(\pm 0.21, 1.66, 0)$	$\pm(\pm 0.27, 8.64, 0)$
Se2	$\pm(3.40, \pm 8.19, 0)$ $\pm(4.32, \pm 8.86, 0)$	$\pm(2.19, \pm 2.18, 0)$ $\pm(2.18, \pm 6.88, 0)$	$\pm(1.21, \pm 6.01, 0)$ $\pm(2.18, \pm 6.88, 0)$	$\pm(5.59, \pm 10.37, 0)$ $\pm(6.46, \pm 11.84, 0)$

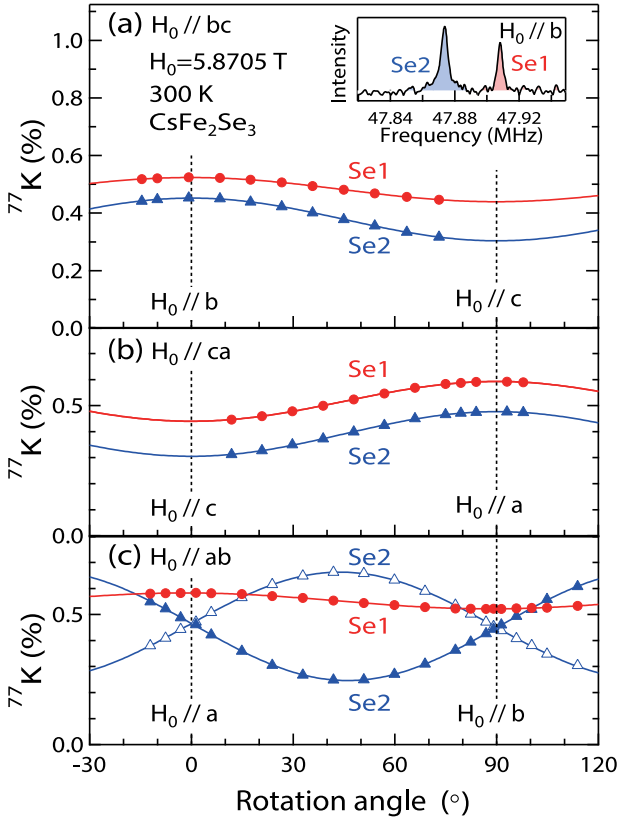


FIG. 6. Angular dependencies of the ^{77}Se Knight shift ^{77}K at 300 K measured with $H_0 = 5.8705$ T rotated in the (a) bc , (b) ca , and (c) ab planes of the CsFe_2Se_3 single crystal. The inset shows the ^{77}Se NMR spectrum for $H_0 \parallel b$. The solid curves are the results of the data fitted to Eq. (2) with the Knight shift values listed in Table III.

rotated in the bc , ca , and ab planes, as depicted in Fig. 6. The spectrum for $H_0 \parallel ab$ is composed of one Se1 and two Se2 spectra, while the spectra for $H_0 \parallel bc$ and $H_0 \parallel ca$ have one Se1 and one Se2 spectra.

By fitting the experimental data to Eq. (2), we can obtain the principal values $^{77}K_{xx}$, $^{77}K_{yy}$, and $^{77}K_{zz}$, which are listed with the isotropic Knight shift $^{77}K_{\text{iso}}$, axially anisotropic Knight shift $^{77}K_{\text{ax}}$, and in-plane anisotropic Knight shift $^{77}K_{\text{aniso}}$ for the Se1 and Se2 sites in Table III. The principal x , y , and z axes for the Se1 site are the a , b , and c axes, respectively, whereas the y axis is the c axis and the z (x) axis is located at $\pm 44.0^\circ$ ($\mp 46.0^\circ$) from the a axis in the ab plane for the Se2 site. Figures 7(a) and 7(b) show the T dependencies of the ^{77}Se Knight shifts for Se1 and Se2, respectively. All the principal components

TABLE III. ^{77}Se Knight shifts $^{77}K_{xx}$, $^{77}K_{yy}$, and $^{77}K_{zz}$ and isotropic one $^{77}K_{\text{iso}}$, axially anisotropic one $^{77}K_{\text{ax}}$, and in-plane anisotropic one $^{77}K_{\text{aniso}}$ at 300 K for the Se1 and Se2 sites in CsFe_2Se_3 . All the Knight shifts are given as percentages.

Site	$^{77}K_{xx}$	$^{77}K_{yy}$	$^{77}K_{zz}$	$^{77}K_{\text{iso}}$	$^{77}K_{\text{ax}}$	$^{77}K_{\text{aniso}}$
Se1	0.585	0.524	0.440	0.516	-0.038	-0.031
Se2	0.244	0.305	0.673	0.407	0.133	0.031

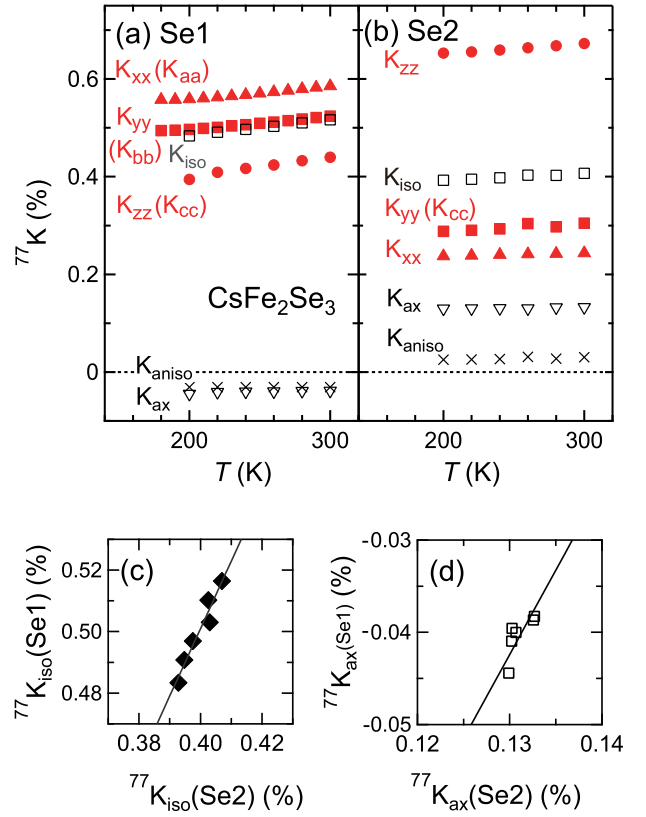


FIG. 7. Temperature dependencies of the ^{77}Se Knight shifts $^{77}K_{xx}$, $^{77}K_{yy}$, $^{77}K_{zz}$, $^{77}K_{\text{iso}}$, $^{77}K_{\text{ax}}$, and $^{77}K_{\text{aniso}}$ for the (a) Se1 and (b) Se2 sites in the CsFe_2Se_3 single crystal. (c) $^{77}K_{\text{iso}}(\text{Se1})$ versus $^{77}K_{\text{iso}}(\text{Se2})$ and (d) $^{77}K_{\text{ax}}(\text{Se1})$ versus $^{77}K_{\text{ax}}(\text{Se2})$ plots with temperature as an implicit parameter. The solid lines are the results of the data fitted to the relation $^{77}K_w(\text{Se1}) = c_1 ^{77}K_w(\text{Se2}) + c_2$ ($w = \text{iso}$ and ax), where c_1 and c_2 are constants.

of the Knight shift tensors are positive and decrease with decreasing T .

Figure 8 shows the T dependence of the ^{77}Se NMR spectrum with $H_0 = 11.4985$ T parallel to the b axis. As T decreases in the PM phase, the Se1 and Se2 spectra move to lower frequencies with the broadening of the spectrum width, as shown in the inset of Fig. 8. Below T_{N1} , the spectra disappear, possibly due to the spectrum broadening from the incommensurate spin structure discussed in Sec. IV C. However, the sharp spectra appear again below T_{N2} . The Se1 spectrum is split into two lines, whereas the Se2 spectrum is composed of four lines. The Se spectra show angular dependencies for H_0 rotations. The resonance frequencies ν_{res} with $H_0 = 11.4985$ T rotated in the bc and ab planes at 120 K in the AFM2 phase are presented in Figs. 9(a) and 9(b), respectively. Notably, each of the two Se1 spectra and four Se2 spectra is slightly split into two lines. The angular dependence of ν_{res} can be well fitted to Eq. (3). From the analysis mentioned above, we obtained the experimental results of H_{in} for the Se1 and Se2 sites listed in Table II. As shown in Table II and Fig. 9(c), the Se1 site has four vectors of $H_{\text{in}} = 5.16$ kOe parallel to the directions of $\theta_{c,0} = \pm 87.3^\circ$, $\pm 92.7^\circ$ in the ab plane. Thus, the internal fields are almost parallel or antiparallel to the

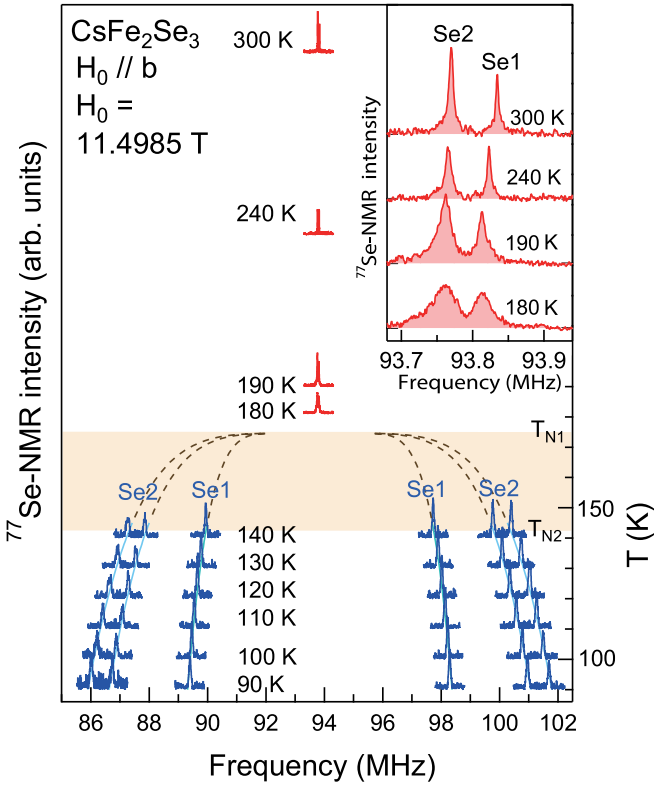


FIG. 8. Temperature dependence of the ^{77}Se NMR spectrum with $H_0 = 11.4985$ T applied parallel to the b axis in the CsFe_2Se_3 single crystal. The inset shows the NMR spectra expanded in the paramagnetic phase. The NMR spectrum is wiped out in the AFM1 phase. The curves follow the temperature dependence of the sublattice magnetization [see Fig. 4(a)].

b axis. However, the Se2 site has eight H_{in} vectors, which are divided into two groups with $H_{\text{in}} = 9.86$ and 8.87 kOe parallel to the directions at $\theta_{c,0} = \pm 64.0^\circ, \pm 116.0^\circ$ and $\theta_{c,0} = \pm 67.5^\circ, \pm 112.5^\circ$, respectively, in the ab plane. Each group is composed of four vectors connected to each other as shown in Fig. 9(c).

IV. ANALYSIS AND DISCUSSION

A. Site symmetry and transferred hyperfine field

Based on the Knight shift tensors given above, we discuss the microscopic interactions that govern them. The P ($P = \text{Cs, Se1, and Se2}$) site has Knight shift tensor $\mathbf{K}(P)$, which is expressed as

$$\mathbf{K}(P) = \frac{1}{N\mu_B} [\mathbf{A}_{\text{TH}}(P) + \mathbf{A}_{\text{dip}}(P) + \mathbf{A}_L + \mathbf{A}_{\text{demag}}] \chi + \mathbf{K}_{\text{chem}}(P), \quad (4)$$

where N is Avogadro's number and μ_B is Bohr magneton. Furthermore, $\mathbf{A}_{\text{TH}}(P)$ is the coupling tensor of the TH field from the neighboring Fe sites and $\mathbf{A}_{\text{dip}}(P)$ is the tensor of the dipole field originating from magnetic moments in a Lorentz sphere; it is numerically calculated as $\mathbf{A}_{\text{dip}}(\text{Cs}) = (A_{\text{dip}}^{aa}, A_{\text{dip}}^{bb}, A_{\text{dip}}^{cc}) = (0.12, 0.31, -0.43)$ kOe/ μ_B , $\mathbf{A}_{\text{dip}}(\text{Se1}) = (A_{\text{dip}}^{aa}, A_{\text{dip}}^{bb}, A_{\text{dip}}^{cc}) = (-0.45, 0.02, 0.43)$ kOe/ μ_B , and

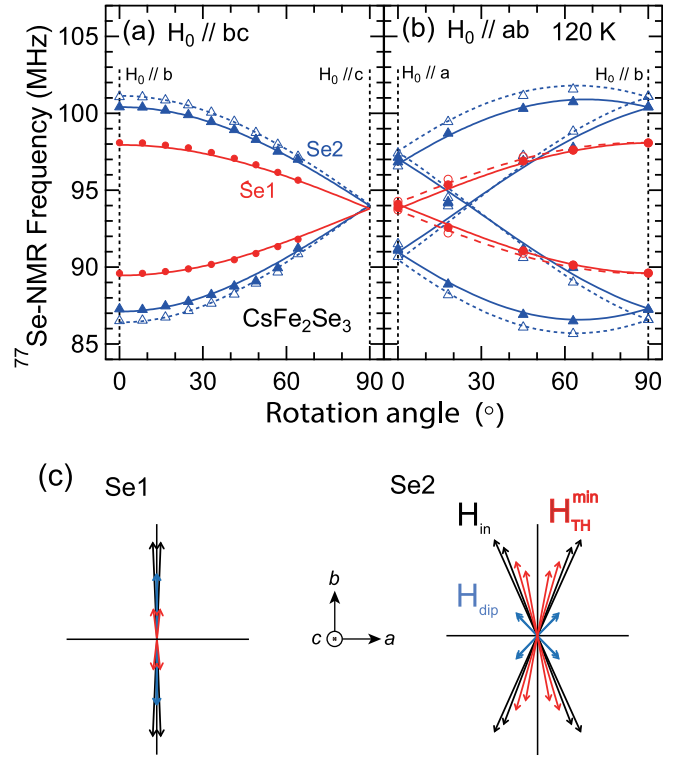


FIG. 9. Angular dependencies of the ^{77}Se NMR frequency at 120 K with $H_0 = 11.4985$ T rotated in the (a) bc and (b) ab planes in the CsFe_2Se_3 single crystal. (c) Internal fields (black arrows) H_{in} , dipole fields (blue arrows) H_{dip} calculated for the spin structure in Fig. 13(a), and transferred hyperfine fields $H_{\text{TH}}^{\text{min}}$ (red arrows) at the Se1 and Se2 sites. The curves are the results of the data fitted to Eq. (3) with the internal fields listed in Table II.

$\mathbf{A}_{\text{dip}}(\text{Se2}) = (A_{\text{dip}}^{zz}, A_{\text{dip}}^{yy}, A_{\text{dip}}^{cc}) = (-1.75, 1.59, 0.16)$ kOe/ μ_B from the crystal structure [6], where the y and z axes are in the ab plane. The tensor due to the Lorentz field is expressed as $\mathbf{A}_L = 4\pi\mu_B\mathbf{E}/(3v) = A_L\mathbf{E}$ with the unit tensor \mathbf{E} , volume of a unit cell v , and $A_L = 0.24$ kOe/ μ_B . The tensor originating from the demagnetization field $\mathbf{A}_{\text{demag}}$ is expressed as $\mathbf{A}_{\text{demag}} = (A_{\text{demag}}^{aa}, A_{\text{demag}}^{bb}, A_{\text{demag}}^{cc}) = (0, -3A_L, 0)$ for CsFe_2Se_3 with a sheetlike plane. Notably, χ is the magnetic susceptibility tensor, and \mathbf{K}_{chem} is the chemical shift tensor.

Among the tensors, \mathbf{A}_{TH} is useful for probing local magnetic and electronic properties. We discuss the TH paths to clarify the relation between the TH tensors at the Cs and Se sites and the site symmetry. In CsFe_2Se_3 , the Cs site is located on the mirror planes parallel to the ab and bc planes, as shown in Fig. 10, and on the twofold rotation axis parallel to the b axis. Note that the twofold rotation can be represented by the two mirror operations. We cannot clearly distinguish which Fe sites strongly contribute to H_{TH} because the TH paths are dependent on the bond length, bond angle, and mixing of the orbitals. Here, as discussed in the later Sec. IV C, we reasonably consider that the TH tensor of the Cs site at $y'/b = 0.8382$ [6], where y' is a b component of the atomic position, has contributions from the Fe sites on the nn ($m = 1$) ladders at $y'/b = 1$ via the TH coupling tensors $\mathbf{A}_j^{(1),i}$ ($i = 1-4$) and

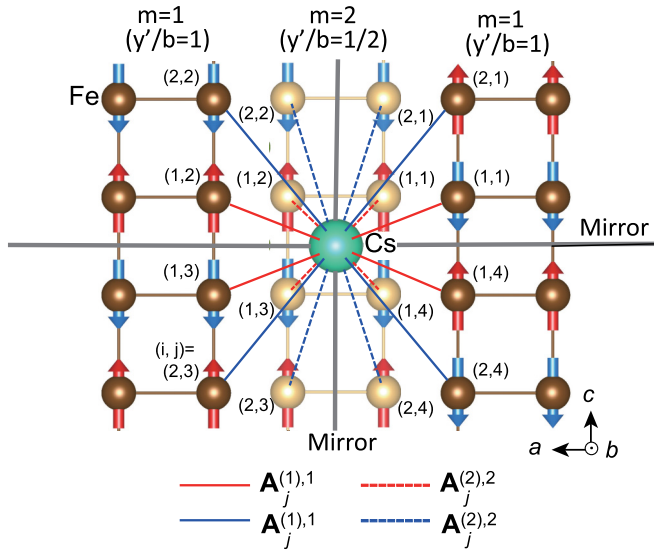


FIG. 10. Transferred hyperfine paths between the Cs site and neighboring Fe sites via the coupling tensor $A_j^{(m),i}$ ($m, i = 1, 2$ and $j = 1-4$) viewed from the b axis. The Cs site at $y'/b = 0.8382$ [6] has Fe sites at the (i, j) th position on two nearest-neighbor ($m = 1$) ladders at $y'/b = 1$ and one next-nearest-neighbor ($m = 2$) ladder at $y'/b = 1/2$. They are divided into four groups, and each group has four ($j = 1-4$) Fe sites connected by the site symmetry at the nearest-neighbor ($i = 1$) or next-nearest-neighbor ($i = 2$) Fe positions on each ladder. The gray lines represent the mirror planes parallel to the ab and bc planes for the crystal structure. The red and blue arrows represent the spin structure in the AFM2 phase displayed in Fig. 13(a).

on the nnn ($m = 2$) ladder at $y'/b = 1/2$ via $A_j^{(2),i}$, as shown in Fig. 10. Notably, this limitation of the TH paths does not affect our conclusions from the analysis of the TH fields, although the values of the TH coupling constants are slightly dependent on this limitation. The Fe sites are divided into four groups with the TH tensors $A_j^{(m),i}$ ($m, i = 1, 2$) different from each other. Each group in which there are nn ($i = 1$) or nnn ($i = 2$) Fe sites on each ladder has four ($j = 1-4$) Fe sites connected by the site symmetry. Thus, as described in the Appendix, we can obtain the TH tensor of the Cs site in a unit cell $A_{\text{TH}}(\text{Cs})$, expressed as

$$A_{\text{TH}}(\text{Cs}) = \sum_{m=1}^2 \sum_{i=1}^2 \sum_{j=1}^4 A_j^{(m),i}$$

$$= 4 \sum_{m=1}^2 \sum_{i=1}^2 \begin{pmatrix} A_{aa}^{(m),i} & 0 & 0 \\ 0 & A_{bb}^{(m),i} & 0 \\ 0 & 0 & A_{cc}^{(m),i} \end{pmatrix}. \quad (5)$$

Similarly, the Se1 sites on the mirror planes parallel to the ab and bc planes and on the twofold rotation axis parallel to the b axis interact with their Fe neighbors, as presented in Fig. 11. The TH tensor of the Se1 site originates from the Fe sites on the nn ($m = 1$) ladder via one TH coupling tensor $B_j^{(1),i}$ ($i = 1, 2$ and $j = 1-4$) and on two nnn ($m = 2$) ladders via $B_j^{(2),i}$. Thus, we obtain the TH tensor of the Se1 site in a unit cell $A_{\text{TH}}(\text{Se1})$

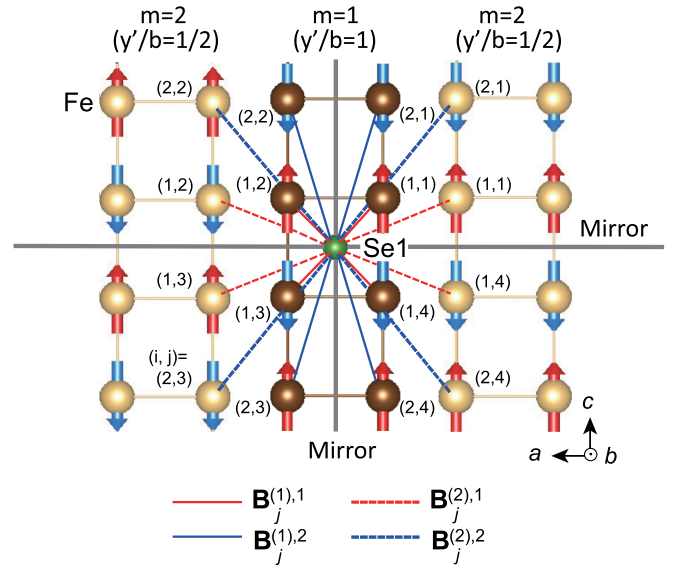


FIG. 11. Transferred hyperfine paths between the Se1 site and neighboring Fe sites via the coupling tensor $B_j^{(m),i}$ ($m, i = 1, 2$ and $j = 1-4$) viewed from the b axis. The Se1 site at $y'/b = 0.8767$ [6] has Fe sites at the (i, j) th position on one nearest-neighbor ($m = 1$) ladder at $y'/b = 1$ and two next-nearest-neighbor ($m = 2$) ladders at $y'/b = 1/2$. They are divided into four groups, and each group has four ($j = 1-4$) Fe sites connected by the site symmetry at nearest-neighbor ($i = 1$) or next-nearest-neighbor ($i = 2$) Fe positions on each ladder. The gray lines represent the mirror planes parallel to the ab and bc planes for the crystal structure. The red and blue arrows represent the spin structure in the AFM2 phase displayed in Fig. 13(a).

expressed as

$$A_{\text{TH}}(\text{Se1}) = \sum_{m=1}^2 \sum_{i=1}^2 \sum_{j=1}^4 B_j^{(m),i}$$

$$= 4 \sum_{m=1}^2 \sum_{i=1}^2 \begin{pmatrix} B_{aa}^{(m),i} & 0 & 0 \\ 0 & B_{bb}^{(m),i} & 0 \\ 0 & 0 & B_{cc}^{(m),i} \end{pmatrix}. \quad (6)$$

However, the Se2 site on the mirror plane parallel to the ab plane has Fe sites on the nn ($m = 1$) ladder via the TH tensor $C_j^{(1),i}$ ($i, j = 1, 2$), nnn ($m = 2$) ladder via $C_j^{(2),i}$ and other ($m = 3$) ladder via $C_j^{(3),i}$, as shown in Fig. 12. Thus, the TH tensor of the Se2 site in a unit cell $A_{\text{TH}}(\text{Se2})$ is written as

$$A_{\text{TH}}(\text{Se2}) = \sum_{m=1}^3 \sum_{i=1}^2 \sum_{j=1}^2 C_j^{(m),i}$$

$$= 2 \sum_{m=1}^3 \sum_{i=1}^2 \begin{pmatrix} C_{aa}^{(m),i} & a_1 C_{ab}^{(m),i} & 0 \\ a_1 C_{ba}^{(m),i} & C_{bb}^{(m),i} & 0 \\ 0 & 0 & C_{cc}^{(m),i} \end{pmatrix}, \quad (7)$$

where there are two Se2 positions with $A_{\text{TH}}(\text{Se2})$ as expressed by Eq. (7). $a_1 (= \pm 1)$ originates from the two Se2 positions at both sides of a ladder, where the local symmetry axes are different from each other.

Finally, we compare the $A_{\text{TH}}(P)$ tensors with the $\mathbf{K}(P)$ tensors that were experimentally determined. Equations (5)

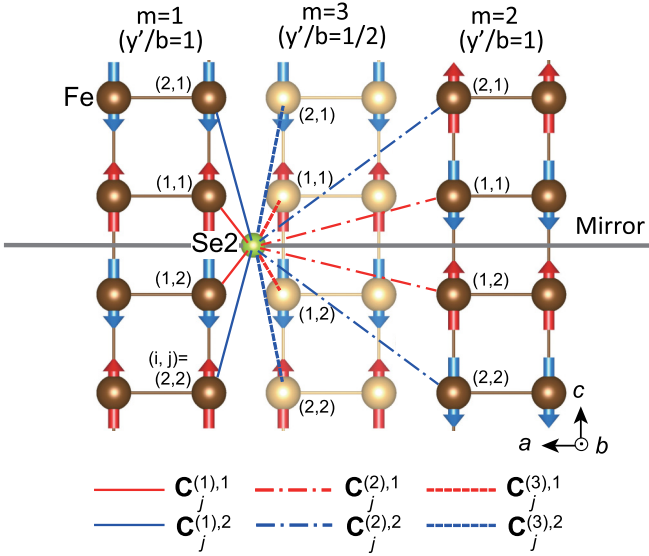


FIG. 12. Transferred hyperfine paths between the Se2 site and neighboring Fe sites via the coupling tensor $\mathbf{C}_j^{(m),i}$ ($m, i, j = 1, 2$) viewed from the b axis. The Se2 site at $y'/b = 0.8882$ [6] has Fe sites at the (i, j) th position on nearest-neighbor ($m = 1$) and next-nearest-neighbor ($m = 2$) ladders at $y'/b = 1$ and the other ($m = 3$) ladder at $y'/b = 1/2$. They are divided into six groups, and each group has two ($j = 1, 2$) Fe sites connected by the site symmetry at nearest-neighbor ($i = 1$) or next-nearest-neighbor ($i = 2$) Fe positions on each ladder. The gray line represents the mirror plane parallel to the ab plane for the crystal structure. The red and blue arrows represent the spin structure in the AFM2 phase displayed in Fig. 13(a).

and (6) require that the a , b , and c axes are the principal axes for the Cs and Se1 sites, whereas Eq. (7) indicates that the c axis is expected to be a principal axis with the others in the ab plane. The site symmetry also requires the same anisotropy for the dipole tensor. Furthermore, the two ^{77}Se NMR spectra for $H_0 \parallel ab$ in Fig. 6(c) originate from $a_1 = \pm 1$. Thus, the experimental results listed in Table III are consistent with the $\mathbf{K}(P)$ tensors governed by the site symmetry and local structure.

B. Location of doped holes

CsFe_2Se_3 formally has a $\text{Fe}^{2.5+}$ mixed-valent state, leading to electron itinerancy conflicting with the observed insulating behavior. From the photoemission experiment, a hole was proposed to be doped into a $4p$ orbital of Se1, which forms a molecular orbital with the Fe $3d$ orbitals [6]. We discuss this model in terms of the Se NMR results. The hyperfine coupling constants are ascribed to the TH fields via the mixing between the Fe and Se orbitals. In this study, a slight magnetic impurity, which covers the intrinsic χ , prevented determination of the $\mathbf{A}_{\text{TH}}(P)$ tensors from the conventional K versus χ plots for CsFe_2Se_3 . However, the isotropic A_{iso} term indicated the presence of hybridization between the Fe $3d$ and Se s orbitals. Furthermore, the axially anisotropic A_{ax} term provides information on the fraction of the Se $4p$ orbital polarization via the mixing between Fe $3d$ and Se $4p$ orbitals for the Se1 site. We consider only the nn Fe sites as they are the main contributors to the TH fields, based on

Eqs. (6) and (7). The slope of the $K_{\text{iso}}(\text{Se1})$ versus $K_{\text{iso}}(\text{Se2})$ plot with T as an implicit parameter in Fig. 7(c) provides $dK_{\text{iso}}(\text{Se1})/dK_{\text{iso}}(\text{Se2}) = 2B_{\text{iso}}^{(1)}/C_{\text{iso}}^{(1)} = 2.2$, where $B_{\text{iso}}^{(1)}$ ($C_{\text{iso}}^{(1)}$) is the isotropic TH coupling constant between the Se1 (Se2) and nn Fe sites. This indicates that the hybridization between the Fe $3d$ and Se s orbitals is almost the same for Se1 and Se2. Similarly, after subtracting the A_{dip} and A_{demag} terms from the value of $dK_{\text{ax}}(\text{Se1})/dK_{\text{ax}}(\text{Se2}) = 1.8$, as shown in Fig. 7(d), we obtain $A_{\text{TH,ax}}(\text{Se1}) - A_{\text{TH,ax}}(\text{Se2}) \sim 0.4 \text{ kOe}/\mu_{\text{B}}$, which is much less than the Hartree-Fock value of the hyperfine coupling constant $A_{4p} = 183 \text{ kOe}/\mu_{\text{B}}$ for the fully polarized $4p$ orbital [33,34]. This means that there is no large difference between $B_{\text{ax}}^{(1)}$ and $C_{\text{ax}}^{(1)}$, where $B_{\text{ax}}^{(1)}$ ($C_{\text{ax}}^{(1)}$) is the axially anisotropic TH coupling constant between the Se1 (Se2) site and its nn Fe sites. Thus, we can conclude that one hole is not doped into the Se1 and Se2 sites and is instead likely doped into the Fe $3d$ orbitals. If one hole is doped into two Fe sites along a leg, the direct mixing of the neighboring Fe $3t_{2g}$ orbitals in the edge-shared tetrahedron may form molecular orbitals as has also been reported by a previous x-ray absorption study [22]. If $\text{Fe}^{2.5+}$ is in the low-spin state ($e_g^4 t_{2g}^{1.5}$) and the t_{2g} orbital is split due to a lower crystal field, the double exchange mechanism may be active between the neighboring Fe sites and result in an FM exchange interaction that leads to the FM configuration between the Fe spins observed by the neutron scattering [6].

C. Spin structure

Here we discuss the spin structure in the magnetically ordered phases of CsFe_2Se_3 in terms of the NMR results obtained in the present study. The internal field $\mathbf{H}_{\text{in}}(P) = \mathbf{H}_{\text{TH}}(P) + \mathbf{H}_{\text{dip}}(P)$ ($P = \text{Cs}, \text{Se1}, \text{and Se2}$), where $\mathbf{H}_{\text{TH}}(P)$ is the TH field originating from the neighboring Fe moments of the P site and $\mathbf{H}_{\text{dip}}(P)$ is the classical dipole field at the P site. Here we can neglect the demagnetization field H_{demag} and Lorentz field H_{L} for the following reason. In an AFM phase, both fields under a magnetic field originate from the magnetization induced via magnetic susceptibility rather than from AFM moments. Using a magnetic susceptibility of $\chi = 2 \times 10^{-3} \text{ emu/mol}$ in the AFM2 phase [6], we can evaluate $H_{\text{demag}} = -3A_{\text{L}}\chi H_0 = -9 \text{ Oe}$ and $H_{\text{L}} = A_{\text{L}}\chi H_0 = 3 \text{ Oe}$ for $H_0 = 5.87 \text{ T}$. These values are negligibly insignificant compared with those of the internal fields listed in Table II. $\mathbf{H}_{\text{TH}}(P)$ is expressed as $\mathbf{H}_{\text{TH}}(P) = \sum_m \sum_i \sum_j \mathbf{A}_j^{(m),i}(P) \mathbf{M}_j^{(m),i}$, where the m summation is taken for the neighboring ladders that contribute to H_{TH} , and the i summation is taken for the nn ($i = 1$) and nnn ($i = 2$) Fe sites on the m th ladder, whereas the j summation is made for the j th Fe sites that are connected by site symmetry. $\mathbf{A}_j^{(m),i}(\text{Cs}) = \mathbf{A}_j^{(m),i}$, $\mathbf{A}_j^{(m),i}(\text{Se1}) = \mathbf{B}_j^{(m),i}$, and $\mathbf{A}_j^{(m),i}(\text{Se2}) = \mathbf{C}_j^{(m),i}$. In addition, $\mathbf{M}_j^{(m),i}$ is the magnetic moment at the j th Fe site, which belongs to the i th Fe site on the m th ladder.

From the representative analysis, the spin structure in the AFM2 phase was discussed in Ref. [6]. There are four irreducible representations Γ_k ($k = 1-4$), and each of them has three basis vectors, which implies that there are 12 basis vectors in total ψ_l ($l = 1-12$) for the propagating vector $\mathbf{Q} = (1/2, 1/2, 0)$. Among them, four basis vectors listed in

TABLE IV. Basis vectors (BVs) of irreducible representations (Irrep) Γ_k ($k = 1-4$) for the space group $Cmcm$ with magnetic wave vector $\mathbf{Q} = (1/2, 1/2, 0)$, Fe magnetic moments arranged on a ladder [6], and directions of $H_{in}(Se1)$ and $H_{in}(Se2)$ in $CsFe_2Se_3$. Only basis vectors for which the Fe magnetic moments are parallel or antiparallel to the c axis are selected among the possible ones ψ_l ($l = 1-12$).

Irrep	BV	Spin arrangement	$H_{in}(Se1)$	$H_{in}(Se2)$
Γ_1	ψ_3		$\parallel \pm c$	$\parallel \pm c$
Γ_2	ψ_6		$\perp c$	$\perp c$
Γ_3	ψ_9		$\parallel \pm b$	$\perp c$
Γ_4	ψ_{12}		$(H_{in} = 0)$	$\parallel \pm c$

Table IV are possible because the anisotropy of magnetic susceptibility indicates that the c axis is the easy axis in the AFM2 phase [6]. The direction of H_{in} enables us to identify the spin structure if only the nn Fe magnetic moments in a ladder are considered. From the agreement between the directions determined experimentally and predicted by the representative analysis, the ψ_9 spin structure in Γ_3 is the most suitable spin structure in the AFM2 phase, as can be seen from Table IV, where the directions of H_{in} predicted for the Se1 and Se2 sites are listed. Note that the ψ_7 and ψ_8 basis vectors that belong to Γ_3 were not found to contribute to H_{in} from the same analysis. This result is consistent with those reported in the neutron scattering study [6].

Next, in addition to the TH paths in a ladder, we also consider the ones originating from the Fe sites on its neighboring ladders to clarify the spin arrangement between the ladders. As mentioned in Sec. IV A, we account for the Fe sites on two nn ($m = 1$) and one nnn ($m = 2$) ladders of the Cs site, as shown in Fig. 10. If there are magnetic moments $\mathbf{M}_j^{(m),i}$ represented by the red arrows, $\mathbf{M}_0 = (0, 0, M_0)$, and the blue arrows, $-\mathbf{M}_0$, in Fig. 10, the TH field of the Cs site $H_{TH}(Cs)$ in a magnetic unit cell can be written as

$$\begin{aligned}
 \mathbf{H}_{TH}(Cs) &= \sum_{m=1}^2 \sum_{i=1}^2 \sum_{j=1}^4 \mathbf{A}_j^{(m),i} \mathbf{M}_j^{(m),i} \\
 &= 4a_2 \sum_{i=1}^2 (-1)^{i+1} \begin{pmatrix} 0 & 0 & A_{ac}^{(1),i} \\ 0 & 0 & a_3 A_{bc}^{(2),i} \\ A_{ca}^{(1),i} & a_3 A_{cb}^{(2),i} & 0 \end{pmatrix} \mathbf{M}_0 \\
 &= 4a_2 M_0 \sum_{i=1}^2 (-1)^{i+1} (A_{ac}^{(1),i}, a_3 A_{bc}^{(2),i}, 0), \quad (8)
 \end{aligned}$$

where $a_2 (= \pm 1)$ means that there are two Cs positions with the TH fields antiparallel to each other owing to the difference between their local spin arrangements in a magnetic unit cell. Additionally, a_3 is ± 1 for the model of two stripe-type domains with $\mathbf{Q} = (1/2, 1/2, 0)$ and $(1/2, -1/2, 0)$, as shown in Fig. 13(b), and $+1$ or -1 for the model of a single domain.

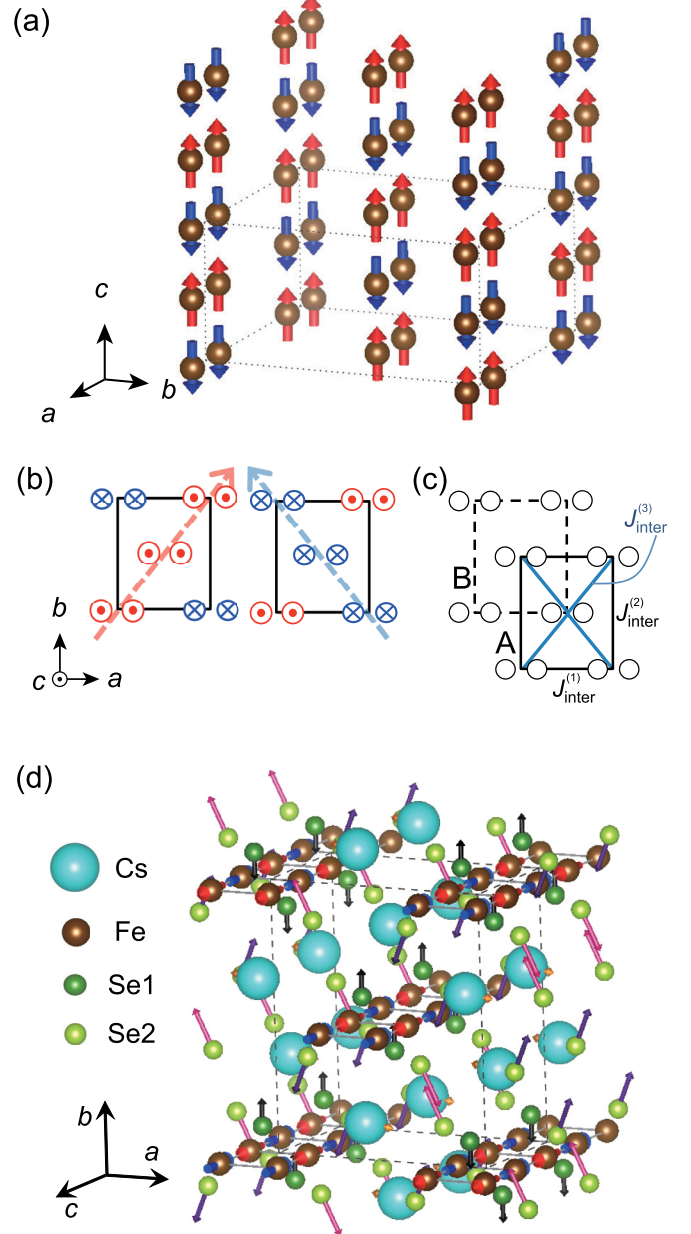


FIG. 13. (a) Spin structure of the AFM2 phase of $CsFe_2Se_3$ proposed from a neutron scattering study [6]. (b) Two stripe-type domains with magnetic wave vectors $\mathbf{Q} = (1/2, 1/2, 0)$ and $(1/2, -1/2, 0)$ viewed from the c axis. (c) Two sublattices, A and B, AFM exchange constants between nearest-neighbor ladders in a sublattice $J_{inter}^{(1)}$ and $J_{inter}^{(2)}$, and an exchange constant between nearest-neighbor ladders in two sublattices $J_{inter}^{(3)}$. (d) Possible structures of the internal fields at the Cs, Se1, and Se2 sites for the spin structure model (a) with one domain. The red and blue arrows in (a) and (d) represent the Fe magnetically ordered moments parallel to the c axis, whereas the other arrows in (d) denote the internal fields. Each rectangular parallelepiped represents a structural unit cell.

Thus, four Cs positions are expected to exist due to $a_2 (= \pm 1)$ and $a_3 (= \pm 1)$, for which the choice of sign is independent for the model of two stripe-type domains. Similarly, for the Se1 site, if the TH field of the Se1 site $\mathbf{H}_{TH}(Se1)$ originates from $\mathbf{M}_j^{(1),i}$ ($i = 1, 2$ and $j = 1-4$) on the ladder via $\mathbf{B}_j^{(1),i}$

and $\mathbf{M}_j^{(2),i}$ on the nnn ladders via $\mathbf{B}_j^{(2),i}$, as shown in Fig. 11, $\mathbf{H}_{\text{TH}}(\text{Se1})$ in a magnetic unit cell is expressed as

$$\begin{aligned} \mathbf{H}_{\text{TH}}(\text{Se1}) &= \sum_{m=1}^2 \sum_{i=1}^2 \sum_{j=1}^4 \mathbf{B}_j^{(m),i} \mathbf{M}_j^{(m),i} \\ &= 4a_2 \sum_{i=1}^2 (-1)^{i+1} \begin{pmatrix} 0 & 0 & a_3 B_{ac}^{(2),i} \\ 0 & 0 & B_{bc}^{(1),i} \\ a_3 B_{ca}^{(2),i} & B_{cb}^{(1),i} & 0 \end{pmatrix} \mathbf{M}_0 \\ &= 4a_2 \mathbf{M}_0 \sum_{i=1}^2 (-1)^{i+1} (a_3 B_{ac}^{(2),i}, B_{bc}^{(1),i}, 0), \end{aligned} \quad (9)$$

where $a_2 (= \pm 1)$ means that there are two Se1 positions with the TH fields antiparallel to each other due to the difference between their local spin arrangements in a magnetic unit cell. Additionally, a_3 is ± 1 for the model of two stripe-type domains shown in Fig. 13(b) and $+1$ or -1 for the model of a single domain. However, the TH field of the Se2 site $\mathbf{H}_{\text{TH}}(\text{Se2})$ originates from the j th ($j = 1-4$) magnetic moment $\mathbf{M}_j^{(m),i}$ of the i th neighboring Fe site on the m th ladder via $\mathbf{C}_j^{(m),i}$, as presented in Fig. 12. Thus, $\mathbf{H}_{\text{TH}}(\text{Se2})$ in a magnetic unit cell is expressed as

$$\begin{aligned} \mathbf{H}_{\text{TH}}(\text{Se2}) &= \sum_{m=1}^3 \sum_{i=1}^2 \sum_{j=1}^2 \mathbf{C}_j^{(m),i} \mathbf{M}_j^{(m),i} \\ &= 2a_2 \mathbf{M}_0 \sum_{i=1}^2 (-1)^{i+1} (C_{ac}^{(1),i} - C_{ac}^{(2),i} + a_3 C_{ac}^{(3),i}, \\ &\quad a_1 (C_{bc}^{(1),i} - C_{bc}^{(2),i} + a_3 C_{bc}^{(3),i}), 0), \end{aligned} \quad (10)$$

where a_1 , a_2 , and a_3 are ± 1 and all choices of their signs are independent. If there are two stripe-type domains ($a_3 = \pm 1$), it is expected that there are two groups for the Se2 site, and each group has four positions with the same absolute value of H_{TH} and directions different from each other.

Based on the TH field expected from the site symmetry, we discuss the internal field in the AFM2 phase. We can obtain H_{TH} with the minimum and maximum values listed in Table II and displayed in Figs. 5(d) and 9(c) after subtracting H_{dip} from H_{in} , although the H_{TH} values are not determined due to the unknown signs of the TH coupling constants. The NMR results can be well reproduced, if $|A_{ac}^{(1),1} - A_{ac}^{(1),2}| = 0.37-0.48$ and $|A_{bc}^{(2),1} - A_{bc}^{(2),2}| = 0.01-0.10$ kOe/ μ_B for the Cs site, $|B_{bc}^{(1),1} - B_{bc}^{(1),2}| = 0.28-1.44$ and $|B_{ac}^{(2),1} - B_{ac}^{(2),2}| = 0.04-0.05$ kOe/ μ_B for the Se1 site, and $|\sum_i^2 (-1)^{i+1} (C_{ac}^{(1),i} - C_{ac}^{(2),i} + a_3 C_{ac}^{(3),i})| = 0.40-2.15$ and $|\sum_i^2 (-1)^{i+1} (C_{bc}^{(1),i} - C_{bc}^{(2),i} + a_3 C_{bc}^{(3),i})| = 2.00-3.95$ kOe/ μ_B for the Se2 site. It should be noted that splitting of the Cs, Se1, and Se2 NMR spectra due to $a_3 = \pm 1$ is observed. Thus, we can conclude that the NMR results are well reproduced for the spin-structure model with the two stripe-type domains shown in Fig. 13(b). This domain structure could not be detected by an unpolarized neutron scattering experiment [6]. In the model, there are the AFM exchange interaction along a leg J_{leg} and the FM one along a rung J_{rung} within ladders, leading to the stripe-type order. On the contrary, the interladder exchange interactions between the ladders along the [100] and [010] directions,

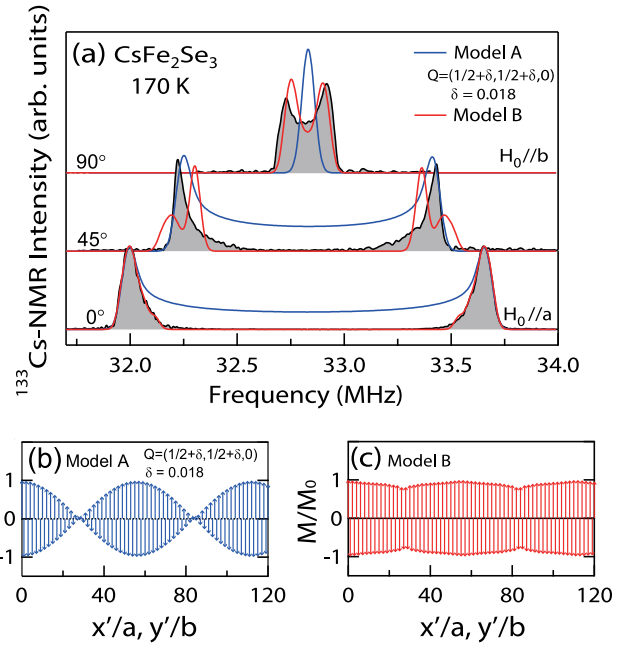


FIG. 14. (a) Calculated ^{133}Cs NMR spectra with $H_0 = 5.8705$ T applied in the ab plane for the incommensurate spin structure perpendicular to the ladder direction with $\mathbf{Q} = (1/2 + \delta, 1/2 + \delta, 0)$ and $\delta = 0.018$ (blue curve, model A) and the incommensurate-like spin structure (red curve, model B) in the AFM1 phase of CsFe_2Se_3 . Distribution of the magnetic moment M/M_0 at the Fe site along the a and b directions for the (b) incommensurate model (model A) and (c) incommensurate-like one (model B). An arrow represents a pair of ferromagnetically coupled Fe moments along a rung. In both models, the AFM spin arrangement on a ladder is assumed to be the same as in the AFM2 phase. The observed NMR spectrum (gray spectrum) at 170 K is compared with the calculated spectra.

$J_{\text{inter}}^{(1)}$ and $J_{\text{inter}}^{(2)}$, respectively, are antiferromagnetic. Thus, if there is an exchange interaction between the ladders along the [110] and $[\bar{1}10]$ directions $J_{\text{inter}}^{(3)}$, there can be magnetic frustration, as presented in Fig. 13(c). This effect provides the cancellation of the exchange fields from the surrounding nn ladders, thereby resulting in no magnetic correlation between the two sublattices A and B. Thus, notably, the two stripe-type domains have the same magnetic energies. Finally, by comparing the present results for H_{in} with the calculated H_{dip} , we can present a possible magnetic structure of H_{in} at the Cs, Se1, and Se2 sites shown in Fig. 13(d) for the spin structure model of the AFM2 phase with one domain, as displayed in Fig. 13(a). The magnetic structure of H_{in} is closely related to the Fe spin arrangement on the nn ladder of each site of interest.

In the AFM1 phase, the Cs NMR spectra in Figs. 5(a)–5(c) show that there is a distribution of H_{in} . The overall angular dependence of the ^{133}Cs NMR spectrum at 170 K similar to that in the AFM2 phase requires $H_{\text{in}}(\text{Cs})$ to be located in the ab plane, and there may be domains. The magnetic frustration mentioned above is also expected to provide an interladder incommensurate magnetic order. To discuss the spin structure in the AFM1 phase, we compare the calculated spectra for two possible models with the experimental NMR spectra for $H_0 \parallel ab$ at 170 K in Fig. 14(a). One model is an incommensurate one (model A), in which the same stripe-type order within

a ladder is present similar to that in the AFM2 phase, and an incommensurate order with $\mathbf{Q} = (1/2 + \delta, 1/2 + \delta, 0)$ and $\delta = 0.018$ between the ladders, as presented in Fig. 14(b). The blue curve calculated for this model shown in Fig. 14(a) is incapable of reproducing of the experimental one. However, the spectra for $H_0 \parallel a$ or b can be reproduced by the red curve calculated for another model, which is the incommensuratelike model (model B), as depicted in Fig. 14(a), if the magnetic moments are phenomenologically introduced for modulation as shown in Fig. 14(c). Furthermore, the deviation between the calculated and experimental spectra in the angular range between the a and b directions may be removed if several domains that provide splitting of the NMR spectrum are present, instead of two. These incommensurate \mathbf{Q} vectors were not observed in a neutron scattering experiment likely owing to the resolution limit [6]. The diffusive peak was observed above T_N at a position slightly off from the $\mathbf{Q} = (1/2, 1/2, 0)$ point of the magnetic diffraction in the long-range order phase of BaFe_2Se_3 [5]. A similar diffusive peak may appear at the incommensurate \mathbf{Q} point near $(1/2, 1/2, 0)$ in CsFe_2Se_3 .

D. Successive magnetic transitions

Here we discuss the successive magnetic transitions at T_{N1} and T_{N2} from a dynamical viewpoint. They can be clearly probed by the ^{133}Cs nuclear spin-lattice relaxation rate $1/T_1$, which is governed by fluctuations in the TH field originating from the neighboring Fe magnetic moments.

In general, $1/T_1$ governed by the fluctuation of the hyperfine field H_{hf} is expressed as [35]

$$\frac{1}{T_1} = \frac{1}{2} \gamma_n^2 \int_{-\infty}^{\infty} \langle \{H_{\text{hf}}^+(t), H_{\text{hf}}^-(0)\} \rangle e^{i\omega_n t} dt, \quad (11)$$

where $H_{\text{hf}}^{\pm}(t) = H_{\text{hf}}^{\alpha}(t) \pm iH_{\text{hf}}^{\beta}(t)$ with α and β directions perpendicular to the external field, $\langle \dots \rangle$ denotes the thermal average, and ω_n is the nuclear Larmor frequency. If \mathbf{H}_{hf} is written as $\mathbf{H}_{\text{hf}} = \mathbf{A}\mathbf{g}\mathbf{S}$ with the hyperfine tensor $\mathbf{A} = (A_{\alpha\beta})$, the g tensor $\mathbf{g} = (g_{\alpha\beta}) = (g_{aa}, g_{bb}, g_{cc})$, and the spin operator \mathbf{S} , $1/T_1$ for $H_0 \parallel a$, $(1/T_1)_a$, is expressed as [36]

$$\begin{aligned} \left(\frac{1}{T_1}\right)_a &= \frac{\gamma_n^2}{2N} \sum_{\mathbf{q}} \{ [|A_{bb}(\mathbf{q})|^2 + |A_{bc}(\mathbf{q})|^2] g_{bb}^2 S_{bb}(\mathbf{q}, \omega_n) \\ &+ [|A_{bc}(\mathbf{q})|^2 + |A_{cc}(\mathbf{q})|^2] g_{cc}^2 S_{cc}(\mathbf{q}, \omega_n) \\ &+ [|A_{ab}(\mathbf{q})|^2 + |A_{ac}(\mathbf{q})|^2] g_{aa}^2 S_{aa}(\mathbf{q}, \omega_n) \}, \quad (12) \end{aligned}$$

where $S_{\alpha\alpha}(\mathbf{q}, \omega)$ ($\alpha = a, b, c$) is the wave vector \mathbf{q} component of the dynamical spin correlation function. Expressions for $(1/T_1)_b$ and $(1/T_1)_c$ are obtained by cyclic permutation of a , b , and c .

We focus our attention on the T range near T_N , where the spin fluctuation is enhanced at $\mathbf{q} \sim \mathbf{Q}$. If we assume AFM fluctuation with $\mathbf{Q} = (1/2, 1/2, 0)$ and the ψ_9 -type spin structure displayed in Fig. 13(a) for CsFe_2Se_3 , the \mathbf{Q} component of the TH tensor for the Cs site $\mathbf{A}_{\text{TH}}^{(\text{Cs})}(\mathbf{Q})$ must be written as

$$\mathbf{A}_{\text{TH}}^{(\text{Cs})}(\mathbf{Q}) = \begin{pmatrix} 0 & 0 & A_{ac}^{(\text{Cs})}(\mathbf{Q}) \\ 0 & 0 & A_{bc}^{(\text{Cs})}(\mathbf{Q}) \\ A_{ca}^{(\text{Cs})}(\mathbf{Q}) & A_{cb}^{(\text{Cs})}(\mathbf{Q}) & 0 \end{pmatrix}. \quad (13)$$

Because $|A_{bc}^{(\text{Cs})}(\mathbf{Q})/A_{ac}^{(\text{Cs})}(\mathbf{Q})|^2 = 0.002-0.02$ from the TH tensors mentioned above, we can approximately obtain the ^{133}Cs nuclear spin-lattice relaxation rate for the \mathbf{Q} spin fluctuation expressed as

$$\left(\frac{1}{T_1}\right)_a \propto |A_{ac}^{(\text{Cs})}(\mathbf{Q})|^2 g_{aa}^2 S_{aa}(\mathbf{Q}, \omega_n), \quad (14)$$

$$\begin{aligned} \left(\frac{1}{T_1}\right)_b &\propto |A_{ac}^{(\text{Cs})}(\mathbf{Q})|^2 g_{cc}^2 S_{cc}(\mathbf{Q}, \omega_n) \\ &+ |A_{ca}^{(\text{Cs})}(\mathbf{Q})|^2 g_{aa}^2 S_{aa}(\mathbf{Q}, \omega_n), \quad (15) \end{aligned}$$

$$\left(\frac{1}{T_1}\right)_c \propto |A_{ac}^{(\text{Cs})}(\mathbf{Q})|^2 g_{cc}^2 S_{cc}(\mathbf{Q}, \omega_n). \quad (16)$$

Finally, note that $1/T_1$ for $H_0 \parallel [111]$ can monitor both $S_{aa}(\mathbf{Q}, \omega_n)$ and $S_{cc}(\mathbf{Q}, \omega_n)$ because it is an average of $(1/T_1)_a$ and $(1/T_1)_b$.

Based on Eqs. (14)–(16), we discuss the spin fluctuation in the $1/T_1$ data. Note that we can separately obtain information on the α -direction ($\alpha = a, b, c$) spin fluctuation from the $1/T_1$ measurements of several H_0 directions. The $(1/T_1)_{\text{MA}}$ data for H_0 parallel to the magic angle near the $[110]$ direction indicate a divergent behavior with a value of T decreasing toward T_{N1} , whereas in the $(1/T_1)_a$ data such a behavior is not observed, as shown in Fig. 4(b). This means that the dynamical spin correlation in the c direction at the NMR frequency diverges owing to the critical slowing down, whereas fluctuation in the a direction remains finite. This seems to support the model of the stripe-type order within ladders and the incommensuratelike order between ladders due to the magnetic frustration between ladders via $J_{\text{inter}}^{(1)}$ (or $J_{\text{inter}}^{(2)}$) and $J_{\text{inter}}^{(3)}$, as discussed in Sec. IV C. In the critical region near T_{N1} , the critical exponents of $1/T_1$, $\gamma = 0.59$, and the sublattice magnetization $\beta = 0.33$ are comparable to $\gamma = 4/7$ and $\beta = 0.327$ of the three-dimensional Ising model [37,38]. Thus, the spin fluctuation perpendicular to the ladder direction does not prevent the transition from the paramagnetic phase to the three-dimensional long-range ordered phase. The spin fluctuation perpendicular to the direction of the ladder in the AFM1 phase is seen to remain finite and become slower with T decreasing toward T_{N2} from the T dependence of $1/T_1$ as shown in Fig. 4(b). Below T_{N2} , the spin fluctuation suddenly disappears owing to the first-order transition, and a change from the incommensuratelike order to the commensurate AFM order occurs. The successive magnetic transitions may also be related to the magnetic frustration among the interladder exchange interactions, as discussed in Sec. IV B. In the AFM1 phase it may not be perfectly removed and result in the many domains and the presence of spin fluctuation perpendicular to the ladder direction. However, it may be removed by an effect, such as a local structural change, which has not been observed, and the commensurate AFM order is considered to take place with the two stripe-type magnetic domains with $\mathbf{Q} = (1/2, 1/2, 0)$ and $(1/2, -1/2, 0)$ in the AFM2 phase.

From a theoretical viewpoint, Luo *et al.* discussed the magnetic states of AFe_2Se_3 based on the results of a Hartree-Fock study, which was performed using the electronic five-orbital Hubbard model [24]. They obtained a phase diagram dependent on J_H/U and U/W , where J_H is the Hund coupling energy, U is the on-site Coulomb energy, and W is the bandwidth. In the phase diagram there are several magnetic phases dependent on the electronic density n . For $n = 5.75$ approximately corresponding to CsFe_2Se_3 ($n = 5.5$), paramagnetic, stripe-type antiferromagnetic, block-type antiferromagnetic, and ferromagnetic phases appear in the J_H/U versus U/W phase diagram. Furthermore, several magnetic orders may compete near boundaries, thereby resulting in the appearance of the AFM1 phase. Recently, the block-spiral state was proposed for multiorbital Hubbard models as a new state without any competing interactions [39]. Such a state may be able to describe the incommensurate-like order observed in the AFM1 phase of CsFe_2Se_3 .

V. CONCLUSION

We performed NMR measurements on a single crystal to study the magnetic and electronic properties of the two-leg ladder Fe compound CsFe_2Se_3 . Based on the temperature dependencies of the ^{133}Cs and ^{77}Se NMR spectra and the ^{133}Cs nuclear spin-lattice relaxation rate $1/T_1$, two magnetic transitions were found to successively occur at $T_{N1} = 176.5$ K and $T_{N2} = 148.5\text{--}152.0$ K. In particular, the transition at T_{N2} was newly observed by an NMR probe sensitive to changes in magnetic properties. Even in the AFM1 phase newly found in the temperature range of $T_{N2} < T < T_{N1}$, no PM phase was found to coexist with the AFM phase. We analyzed the transferred hyperfine fields at the Cs and Se sites in detail based on the site symmetry. In the AFM1 phase we proposed that the stripe-type spin order in a ladder and the incommensurate-like order occurs due to magnetic frustration between ladders. In the AFM2 phase below T_{N2} , the commensurate stripe-type spin structure proposed from a neutron scattering study occurs with two types of domains with the magnetic wave numbers $\mathbf{Q} = (1/2, 1/2, 0)$ and $(1/2, -1/2, 0)$. The successive magnetic transitions were believed to be attributable to the magnetic frustration effect, which may lead to the presence of two-type domains in the AFM2 phase and the remaining magnetic fluctuation in the AFM1 phase. From the analysis of the Se hyperfine coupling constants, we found no doping of a hole into the Se1 and Se2 sites, whereas we did find doping of a hole into the Fe site. This fact excluded the model of a hole doped into the Se site. Based on the present findings, we proposed molecular orbital and double exchange models for the electronic state.

ACKNOWLEDGMENTS

We would like to thank Y. Ueda, Y. Shimizu, and T. Kohyama for their useful discussion and S. Inoue for technical support. This study was supported by JSPS KAKENHI (Grants No. JP16H04012, No. JP18H01159, No. JP18H04302, No. JP19H01837, No. JP19H04685, No.

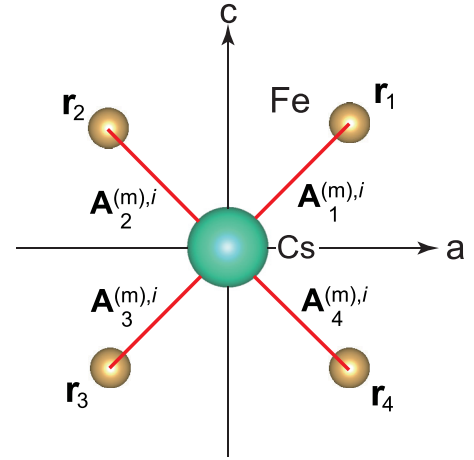


FIG. 15. Transferred hyperfine paths between the Cs site and four neighboring Fe sites at the positions \mathbf{r}_j ($j = 1\text{--}4$) connected by site symmetry. The Cs site is located on the mirror planes parallel to the ab and bc planes. The Cs site at $y'/b = 0.8382$ has the transferred hyperfine tensor $\mathbf{A}_j^{(m),i}$ ($m, i = 1, 2$) originating from the j th Fe site among the four Fe sites connected by the site symmetry. They are located at the nearest-neighbor ($i = 1$) and next-nearest-neighbor ($i = 2$) positions on the $m = 1$ ladders at $y'/b = 1$ and $m = 2$ ladder at $y'/b = 1/2$, as shown in Fig. 10.

JP19H05822, No. JP19H05823, and No. JP19K21837) from the Japan Society for the Promotion of Science (JSPS) and JST CREST (Grant No. JPMJCR1901) from the Japan Science and Technology Agency (JST).

APPENDIX: SITE SYMMETRY

In general, the TH tensor is closely related to site symmetry [33,36,40]. Therefore, analysis based on site symmetry is necessary for obtaining information on the TH interaction.

CsFe_2Se_3 with the orthorhombic structure (space group $Cmcm$) contains the Cs, Se1, and Se2 sites. The Cs site located on the mirror planes parallel to the ab and bc planes has four Fe sites connected by the site symmetry, as shown in Fig. 15. The Cs atom at $y'/b = 0.8382$ has the TH tensors $\mathbf{A}_j^{(m),i}$ originating from the j th ($j = 1\text{--}4$) Fe ion among the four Fe ions connected by the site symmetry at the nearest-neighbor ($i = 1$) and next-nearest-neighbor ($i = 2$) positions on the $m = 1$ ladder at $y'/b = 1$ and $m = 2$ ladder at $y'/b = 1/2$, as shown in Fig. 10. If the TH tensor from one Fe site at position \mathbf{r}_1 in Fig. 15, $\mathbf{A}_1^{(m),i}$, is expressed as

$$\mathbf{A}_1^{(m),i} = \begin{pmatrix} A_{aa}^{(m),i} & A_{ab}^{(m),i} & A_{ac}^{(m),i} \\ A_{ba}^{(m),i} & A_{bb}^{(m),i} & A_{bc}^{(m),i} \\ A_{ca}^{(m),i} & A_{cb}^{(m),i} & A_{cc}^{(m),i} \end{pmatrix}, \quad (\text{A1})$$

then the TH tensor due to the neighboring Fe ion at \mathbf{r}_2 via the mirror operation for the bc plane, $\mathbf{A}_2^{(m),i}$, is

written as

$$\mathbf{A}_2^{(m),i} = \begin{pmatrix} A_{aa}^{(m),i} & -A_{ab}^{(m),i} & -A_{ac}^{(m),i} \\ -A_{ba}^{(m),i} & A_{bb}^{(m),i} & A_{bc}^{(m),i} \\ -A_{ca}^{(m),i} & A_{cb}^{(m),i} & A_{cc}^{(m),i} \end{pmatrix}. \quad (\text{A2})$$

The TH tensors $\mathbf{A}_3^{(m),i}$ and $\mathbf{A}_4^{(m),i}$, which originate from the other two Fe ions at \mathbf{r}_3 and \mathbf{r}_4 , respectively, are similarly obtained as

$$\mathbf{A}_3^{(m),i} = \begin{pmatrix} A_{aa}^{(m),i} & -A_{ab}^{(m),i} & A_{ac}^{(m),i} \\ -A_{ba}^{(m),i} & A_{bb}^{(m),i} & -A_{bc}^{(m),i} \\ A_{ca}^{(m),i} & -A_{cb}^{(m),i} & A_{cc}^{(m),i} \end{pmatrix}, \quad (\text{A3})$$

$$\mathbf{A}_4^{(m),i} = \begin{pmatrix} A_{aa}^{(m),i} & A_{ab}^{(m),i} & -A_{ac}^{(m),i} \\ A_{ba}^{(m),i} & A_{bb}^{(m),i} & -A_{bc}^{(m),i} \\ -A_{ca}^{(m),i} & -A_{cb}^{(m),i} & A_{cc}^{(m),i} \end{pmatrix}. \quad (\text{A4})$$

Thus, $\mathbf{A}_{\text{TH}}^{(m),i}(\text{Cs}) = \sum_{j=1}^4 \mathbf{A}_j^{(m),i}$ can be expressed as

$$\mathbf{A}_{\text{TH}}^{(m),i}(\text{Cs}) = 4 \begin{pmatrix} A_{aa}^{(m),i} & 0 & 0 \\ 0 & A_{bb}^{(m),i} & 0 \\ 0 & 0 & A_{cc}^{(m),i} \end{pmatrix}. \quad (\text{A5})$$

Similarly, the Se1 site interacts with the four neighboring Fe sites connected by the same site symmetry as that of the Cs site via the TH tensor $\mathbf{B}_j^{(m),i}$ ($m, i = 1, 2$ and $j = 1-4$), as shown in Fig. 11. Thus, the TH field of the Se1 site $\mathbf{B}_{\text{TH}}^{(m),i}(\text{Se1}) = \sum_{j=1}^4 \mathbf{B}_j^{(m),i}$ is

written as

$$\mathbf{B}_{\text{TH}}^{(m),i}(\text{Se1}) = 4 \begin{pmatrix} B_{aa}^{(m),i} & 0 & 0 \\ 0 & B_{bb}^{(m),i} & 0 \\ 0 & 0 & B_{cc}^{(m),i} \end{pmatrix}. \quad (\text{A6})$$

However, the Se2 site interacts with the two neighboring Fe sites connected by the site symmetry with the mirror plane parallel to the ab plane via the TH tensor $\mathbf{C}_j^{(m),i}$ ($m, i = 1, 2$ and $j = 1-4$), as shown in Fig. 12. If the TH tensor from one neighboring Fe site is expressed as

$$\mathbf{C}_1^{(m),i} = \begin{pmatrix} C_{aa}^{(m),i} & C_{ab}^{(m),i} & C_{ac}^{(m),i} \\ C_{ba}^{(m),i} & C_{bb}^{(m),i} & C_{bc}^{(m),i} \\ C_{ca}^{(m),i} & C_{cb}^{(m),i} & C_{cc}^{(m),i} \end{pmatrix}, \quad (\text{A7})$$

the TH tensor originating from another neighboring Fe site $\mathbf{C}_2^{(m),i}$ is written as

$$\mathbf{C}_2^{(m),i} = \begin{pmatrix} C_{aa}^{(m),i} & C_{ab}^{(m),i} & -C_{ac}^{(m),i} \\ C_{ba}^{(m),i} & C_{bb}^{(m),i} & -C_{bc}^{(m),i} \\ -C_{ca}^{(m),i} & -C_{cb}^{(m),i} & C_{cc}^{(m),i} \end{pmatrix} \quad (\text{A8})$$

based on the mirror operation for the ab plane. Thus, we obtain $\mathbf{C}_{\text{TH}}^{(m),i}(\text{Se2}) = \sum_{j=1}^2 \mathbf{C}_j^{(m),i}$ expressed as

$$\mathbf{C}_{\text{TH}}^{(m),i}(\text{Se2}) = 2 \begin{pmatrix} C_{aa}^{(m),i} & C_{ab}^{(m),i} & 0 \\ C_{ba}^{(m),i} & C_{bb}^{(m),i} & 0 \\ 0 & 0 & C_{cc}^{(m),i} \end{pmatrix}. \quad (\text{A9})$$

-
- [1] Y. Kamihara, T. Watanabe, M. Hirano, and H. Hosono, *J. Am. Chem. Soc.* **130**, 3296 (2008).
- [2] H. Y. Hong and H. Steinfin, *J. Solid State Chem.* **5**, 93 (1972).
- [3] K. O. Kleep, W. Sparlinek, and H. Boller, *J. Alloys Compd.* **238**, 1 (1996).
- [4] H. Lei, H. Ryu, A. I. Frenkel, and C. Petrovic, *Phys. Rev. B* **84**, 214511 (2011).
- [5] Y. Nambu, K. Ohgushi, S. Suzuki, F. Du, M. Avdeev, Y. Uwatoko, K. Munakata, H. Fukazawa, S. Chi, Y. Ueda, and T. J. Sato, *Phys. Rev. B* **85**, 064413 (2012).
- [6] F. Du, K. Ohgushi, Y. Nambu, T. Kawakami, M. Avdeev, Y. Hirata, Y. Watanabe, T. J. Sato, and Y. Ueda, *Phys. Rev. B* **85**, 214436 (2012).
- [7] H. Takahashi, A. Sugimoto, Y. Nambu, T. Yamauchi, Y. Hirata, T. Kawakami, M. Avdeev, K. Matsubayashi, F. Du, C. Kawashima, H. Soeda, S. Nakano, Y. Uwatoko, Y. Ueda, T. J. Sato, and K. Ohgushi, *Nat. Mater.* **14**, 1008 (2015).
- [8] T. Yamauchi, Y. Hirata, Y. Ueda, and K. Ohgushi, *Phys. Rev. Lett.* **115**, 246402 (2015); **116**, 159901(E) (2016).
- [9] J. Ying, H. Lei, C. Petrovic, Y. Xiao, and V. V. Struzhkin, *Phys. Rev. B* **95**, 241109(R) (2017).
- [10] F. Ma and Z.-Y. Lu, *Phys. Rev. B* **78**, 033111 (2008).
- [11] I. I. Mazin, *Nature (London)* **464**, 183 (2010).
- [12] P. J. Hirschfeld, M. M. Korshunov, and I. I. Mazin, *Rep. Prog. Phys.* **74**, 124508 (2011).
- [13] C. Fang, H. Yao, W.-F. Tsai, J. P. Hu, and S. A. Kivelson, *Phys. Rev. B* **77**, 224509 (2008).
- [14] C. Xu, M. Müller, and S. Sachdev, *Phys. Rev. B* **78**, 020501(R) (2008).
- [15] T. Yildirim, *Phys. Rev. Lett.* **101**, 057010 (2008).
- [16] J. Dai, Q. Si, J. X. Zhu, and E. Abrahams, *Proc. Natl. Acad. Sci. USA* **106**, 4118 (2009).
- [17] M. J. Han, Q. Yin, W. E. Pickett, and S. Y. Savrasov, *Phys. Rev. Lett.* **102**, 107003 (2009).
- [18] R. Yu, Q. Si, P. Goswami, and E. Abrahams, *J. Phys. Conf. Ser.* **449**, 012025 (2013).
- [19] F. Du, Y. Hirata, K. Matsubayashi, Y. Uwatoko, Y. Ueda, and K. Ohgushi, *Phys. Rev. B* **90**, 085143 (2014).
- [20] A. Krzton-Maziopa, E. Pomjakushina, V. Pomjakushin, D. Sheptyakov, D. Chernyshov, V. Shitlyk, and K. Conder, *J. Phys.: Condens. Matter* **23**, 402201 (2011).
- [21] J. M. Caron, J. R. Neilson, D. C. Miller, A. Llobet, and T. M. McQueen, *Phys. Rev. B* **84**, 180409(R) (2011).
- [22] K. Takubo, Y. Yokoyama, H. Wadati, S. Iwasaki, T. Mizokawa, T. Boyko, R. Sutarto, F. He, K. Hashizume, S. Imaizumi, T. Aoyama, Y. Imai, and K. Ohgushi, *Phys. Rev. B* **96**, 115157 (2017).
- [23] T. Hawaii, C. Kawashima, K. Ohgushi, K. Matsubayashi, Y. Nambu, Y. Uwatoko, T. J. Sato, and H. Takahashi, *J. Phys. Soc. Jpn.* **86**, 024701 (2017).

- [24] Q. Luo, A. Nicholson, J. Rincon, S. Liang, J. Riera, G. Alvarez, L. Wang, W. Ku, G. D. Samolyuk, A. Moreo, and E. Dagotto, *Phys. Rev. B* **87**, 024404 (2013).
- [25] Y. Zhang, L. Lin, J.-J. Zhang, E. Dagotto, and S. Dong, *Phys. Rev. B* **95**, 115154 (2017).
- [26] Y. Zhang, L.-F. Lin, J.-J. Zhang, E. Dagotto, and S. Dong, *Phys. Rev. B* **97**, 045119 (2018).
- [27] T. Hawai, Y. Nambu, K. Ohgushi, F. Du, Y. Hirata, M. Avdeev, Y. Uwatoko, Y. Sekine, H. Fukazawa, J. Ma, S. Chi, Y. Ueda, H. Yoshizawa, and T. J. Sato, *Phys. Rev. B* **91**, 184416 (2015).
- [28] D. Ootsuki, N. L. Saini, F. Du, Y. Hirata, K. Ohgushi, Y. Ueda, and T. Mizokawa, *Phys. Rev. B* **91**, 014505 (2015).
- [29] C. Monney, A. Uldry, K. J. Zhou, A. Krzton-Maziopa, E. Pomjakushina, V. N. Strocov, B. Delley, and T. Schmitt, *Phys. Rev. B* **88**, 165103 (2013).
- [30] W. Klemm, H. Sodomann, and P. Langmessaer, *Z. Allg. Anorg. Chem.* **241**, 281 (1939).
- [31] H. Foppl, E. Busmann, and F. K. Frohrath, *Z. Allg. Anorg. Chem.* **314**, 12 (1962).
- [32] A. Abragam, *Principles of Nuclear Magnetism* (Oxford University Press, Oxford, 1961).
- [33] S. Li, S. Kawai, Y. Kobayashi, and M. Itoh, *Phys. Rev. B* **97**, 165127 (2018).
- [34] A. K. Koh and D. J. Miller, *At. Data Nucl. Data Tables* **33**, 235 (1985).
- [35] T. Moriya, *J. Phys. Soc. Jpn.* **19**, 681 (1964).
- [36] K. Nawa, M. Takigawa, M. Yoshida, and K. Yoshimura, *J. Phys. Soc. Jpn.* **82**, 094709 (2013).
- [37] C. Bucci and G. Guidi, *Phys. Rev. B* **9**, 3053 (1974).
- [38] M. Kolesik and M. Suzuki, *Physica A* **215**, 138 (1995).
- [39] J. Herbrych, J. Heverhagen, G. Alvarez, M. Daghofer, A. Moreo, and E. Dagotto, *Proc. Natl. Acad. Sci. USA* **117**, 16226 (2020).
- [40] K. Kitagawa, N. Katayama, K. Ohgushi, M. Yoshida, and M. Takigawa, *J. Phys. Soc. Jpn.* **77**, 114709 (2008).